# First retrieval of absorbing aerosol height over dark target using TROPOMI oxygen B band: Algorithm development and application for surface particulate matter estimates

Xi Chen [a,b,*], Jun Wang [a,b,c,*], Xiaoguang Xu [d], Meng Zhou [b,c], Huanxin Zhang [a,b], Lorena Castro Garcia [a,b], Peter R. Colarco [e], Scott J. Janz [e], John Yorks [e], Matthew McGill [e], Jeffrey S. Reid [f], Martin de Graaf [g], Shobha Kondragunta [h]

[a] Department of Chemical & Biochemical Engineering, The University of Iowa, Iowa City, IA 52242, USA
[b] Center for Global and Regional Environmental Research, and Iowa Technology Institute, The University of Iowa, Iowa City, IA 52242, USA
[c] Interdisciplinary Graduate Program in Geoinformatics, The University of Iowa, Iowa City, IA 52242, USA
[d] Joint Center for Earth Systems Technology, University of Maryland – Baltimore County, Baltimore, MD 21250, USA
[e] NASA Goddard Space Flight Center, Greenbelt, MD 20771, USA
[f] Marine Meteorology Division, U.S. Naval Research Laboratory, Monterey, CA 93943, USA
[g] Royal Netherlands Meteorological Institute (KNMI), De Bilt, Netherlands
[h] Center for Satellite Applications and Research, NOAA/NESDIS, College Park, MD 20740, USA

## ARTICLE INFO

## ABSTRACT

Constraint of the vertical distribution of aerosol particles is crucial for the study of aerosol plume structure, aerosol radiative effects, and ultimately monitoring surface air pollution. We developed an algorithm to retrieve the aerosol optical central height (AOCH) of absorbing aerosols by using, for the first time, the oxygen (O$_2$) A and B absorption band measurements from the TROPOspheric Monitoring Instrument (TROPOMI) over dark targets. For the retrieval, narrow band radiance at seven channels ranging from ultraviolet (UV) to shortwave infrared (SWIR) are convolved from TROPOMI hyperspectral measurements. Subsequently, cloudy pixels are screened out by using the slope of spectral reflectance, while aerosol types (dust and smoke) are classified by the wavelength dependence of aerosol path radiance in conjunction with UV aerosol index. Surface reflectance over land is derived from the MODIS surface bi-directional reflectance climatology, and over water from the GOME-2 surface Lambert-equivalent reflectivity (LER) database. The aerosol optical depth (AOD) and AOCH are retrieved through an approach of look-up-table accounting for AERONET-based dust and smoke optical properties. For multiple smoke and dust plume events around the world, our retrieved AOCH values agree with space-borne lidar CALIOP counterparts, with a mean bias of <0.15 km and a correlation coefficient of 0.85–0.87. Due in part to adding the O$_2$ B band, our retrieval represents an aerosol extinction peak height better than the TROPOMI operational Level 2 aerosol layer height retrieved from only the O$_2$ A band. The latter shows 0.5–2 km low bias, especially over land. Finally, the high potential of AOCH for improving surface PM$_{2.5}$ estimates is also illustrated with a case study in which the high bias of surface PM$_{2.5}$ in MERRA-2 data is corrected after being scaled by the retrieved AOCH.

## 1. Introduction

The vertical distribution of tropospheric aerosols has significant impacts on the efficiency of aerosols affecting atmospheric radiative energy budget and cloud formation (Koch and Del Genio, 2010). It is also a key parameter for translating columnar aerosol loading observed from space, such as aerosol optical depth (AOD), into surface fine particular matter (PM$_{2.5}$) concentrations (Wang and Christopher, 2003). Aerosol particles from local industrial emissions are often well-mixed in the planetary boundary layer, and their concentration usually decays rapidly with altitude in the free troposphere. However, during long transport or for aerosols from other sources, such as dust, biomass

---

burning, and volcanic emissions, aerosols can be elevated with a concentration peak at a high altitude above ground. For instance, soil particles from dust outbreaks can be easily lifted by frontal systems into the free troposphere. The heat release from volcanic emissions and wildfires can lift smoke plumes into the upper free troposphere/lower stratosphere (Christian et al., 2019; Peterson et al., 2014; Xu et al., 2018a). Indeed, the vertical distribution of atmospheric aerosols is regulated by the interaction between meteorological conditions (including wind, atmospheric stability, planetary boundary layer) and particle emission and deposition processes, particle microphysics and so on. Because of the resulting complex interplay, large uncertainty in aerosol vertical profile persists in chemistry transport models at both the global (Koffi et al., 2016) and regional scales (Wang et al., 2013; Yang et al., 2013). Therefore, accurately assessing the spatial and temporal distribution of aerosol height is challenging but critically important.

Satellite remote sensing is one of the most effective ways to characterize the aerosol profiles at the global scale. Space-borne lidar, such as Cloud-Aerosol Lidar with Orthogonal Polarization (CALIOP) (Winker et al., 2013; Winker et al., 2009), is able to provide the detailed structure of aerosol extinction from backscattering measurements. The high vertical resolution of the lidar product, however, is coupled with low spatial coverage due to the lidar's narrow field of view and wide orbit gap. To gain greater coverage, the community is turning to passive remote sensing techniques to derive aerosol layer height (ALH) information from reflected and scattered solar radiance over larger area. The satellite-observed solar spectrum reflected by the Earth and scattered by the atmosphere is sensitive to ALH at different channels, such as ultraviolet (UV) and infrared or thermal bands. The spectral characteristics in these channels make it possible to retrieve ALH from space (Lyapustin et al., 2020; Wu et al., 2016). One promising passive remote sensing technique to retrieve ALH makes use of the absorption bands of atmospheric gas, such as oxygen ($O_2$), whose vertical distribution is often stable and not affected by anthropogenic emissions (Zeng et al., 2008). When considering aerosol scattering in $O_2$ absorption bands, a photon travels a longer path when aerosols are present at low altitude than at high altitude, leading to less backscattered radiance in satellite measurements because of more absorption by $O_2$ (Ding et al., 2016; Wang et al., 2014; Xu et al., 2019). Some theoretical analysis demonstrated that the independent information for aerosol profiles contained in satellite observed narrow-band reflectance inside and outside $O_2$ absorption channels are limited, making it hard to retrieve aerosol extinction characteristics with high vertical resolution (Gabella et al., 1999; Timofeyev et al., 1995). Sensitivity studies by Corradini and Cervino (2006) and Hollstein and Fischer (2014) revealed that the retrieval accuracy and vertical resolution generally benefit from higher spectral resolution. Therefore, the spectrum in the $O_2$ A absorption band (760 nm) observed by the SCanning Imaging Absorption spectroMeter for Atmospheric CHartographY (SCIAMACHY) with ~0.4 nm resolution is helpful for aerosol profile retrieval, and Kokhanovsky and Rozanov (2010) successfully derived the top height of a homogeneous-extinction dust layer through spectral fitting from SCIAMACHY. The absorption bands of dimer of oxygen ($O_2-O_2$) also contain similar information for inferring ALH. Compared with those absorption bands in UV, the 477 nm band has a stronger $O_2-O_2$ absorption and weaker Rayleigh scattering and, hence, is more sensitive to a change of ALH. On the other hand, given that the aerosol information will be improved when the surface albedo decreases, low surface reflectance at 477 nm is conducive to ALH retrieval as well. Thus, the $O_2-O_2$ 477 nm band has been used to derive ALH from measurements of the new Geostationary Environment Monitoring Spectrometer (GEMS), launched in February 2020, whose algorithm was also applied in retrieval experiments using Ozone Monitoring Instrument (OMI) measurements (Chimot et al., 2017; Park et al., 2016). Similarly, the lower surface reflectance in the $O_2$ B absorption band around 688 nm, especially for vegetation, has advantages in ALH retrieval when compared with the $O_2$ A band, even though its $O_2$ absorption is weaker. On the other hand, the chlorophyll fluorescence

cannot be ignored in the $O_2$ A band to avoid biases in aerosol retrieval (Sanders and de Haan, 2013), but it has little impact on $O_2$ B band radiation. Following a previous study using the measured reflectance ratio of inside to outside the $O_2$ A band (Dubuisson et al., 2009), we have developed an ALH retrieval algorithm combining the reflectance ratios from both the $O_2$ A and B bands and applied it to EPIC/DSCOVR observations (Xu et al., 2017; Xu et al., 2019). However, with its coarse spatial resolution (pixel size over 10 km), EPIC pixels are often contaminated by clouds, yielding few cloud-free pixels for retrieving ALH.

In this study, we develop, for the first time, an algorithm to retrieve ALH using radiance observations in the $O_2$ B band from the TROPOspheric Monitoring Instrument (TROPOMI) onboard the Sentinel 5 Precursor (S5P) satellite. Aimed at monitoring daily concentrations of trace gases and aerosols at high spatial resolution globally, TROPOMI/S5P is a relatively new instrument that was successfully launched in October 2017 and has been providing atmospheric composition products since April 2018. TROPOMI measures the hyperspectral Earth-reflected solar radiation at the top of the atmosphere (TOA) covering UV to shortwave infrared (SWIR) bands, including both the $O_2$ A and B absorption bands. Considering 2–3 degrees of freedom for signal (DFS) of aerosol profiles in the troposphere are provided by SCIAMACHY (Colosimo et al., 2016; Corradini and Cervino, 2006), the similar spectral resolution of TROPOMI (0.35 nm) indicates that the retrievable aerosol profile parameters are limited as well. As a result, the current operational algorithm of TROPOMI using the $O_2$ A band spectrum through an optimal estimation method retrieves only a single profile parameter, the middle pressure of the aerosol layer (Nanda et al., 2020). In this algorithm (hereafter called the ALH-$O_2$A algorithm), aerosols are assumed to be uniformly distributed within a single layer that is 50 hPa in pressure thickness. However, the aerosol backscattering vertical distribution measured from the Mini MicroPulse Lidar in the study by Zeng et al. (2018) shows a Gaussian-like shape, and the sensitivity study of the ground-based aerosol profile retrieval finds that assuming a Gaussian a priori profile gives better retrieval accuracy than other profile shapes (Xing et al., 2017). Actually, the Gaussian aerosol profiles described by two parameters have been used in many retrieval algorithms to reduce the number of parameters in the state vector meanwhile to approximate aerosol vertical shape closer to reality (O'Dell et al., 2018; Xu et al., 2017; Xu et al., 2019; Zeng et al., 2020). According to the recent global one-year (2018–2019) assessment of TROPOMI operational ALH-$O_2$A retrievals against the CALIOP-based AOCH data that was computed as the mean altitude weighted by aerosol extinction at each layer, Nanda et al. (2020) indicated that operational algorithm retrieves lower ALH compared to CALIOP, by ~2 km over land and ~ 0.5 km over ocean. Over ocean and dark land, the main difference is attributed to the difference in the sensor sensitivity to aerosol layers, centroid for TROPOMI, top of the plume for CALIOP. When the surface becomes brighter, a bias towards the surface is found, which increases as the surface reflectance increases. A similar comparison for the 2018 North American fires indicates that this bias also strongly depends on the thickness of the smoke plume, which controls the relative contribution of the satellite signal from the surface (Griffin et al., 2020). For instance, −2.1 km bias of ALH-$O_2$A is found for thin plumes, but that is reduced to only −0.7 km on average for plumes thicker than 1.5 km. These results were confirmed by the Multi-angle Imaging SpectroRadiometer (MISR) stereoscopic plume height retrievals as well (Griffin et al., 2020).

A number of attempts to overcome this problem of surface interference have been tried in the ALH-$O_2$A algorithm, such as fitting the surface albedo in the retrieval (Sanders et al., 2015), or dynamically scaling the instrument noise to those parts of the spectrum that are more sensitive to aerosol scattering and less sensitive to the reflectance from the bright surfaces (Nanda et al., 2018). While the dynamic scaling method was successful in principle, the accuracy improvement was low. This motivates us to take the $O_2$ B band into consideration. Actually, as shown from the United States Geological Survey (USGS) Spectral Library

version 7 (Kokaly et al., 2017), most land surface classes present lower surface reflectance in the $O_2$ B band than in the $O_2$ A band, especially for vegetated surface ("dark target"), whose surface albedo are almost smaller than 0.1 in the $O_2$ B band but always larger than 0.2 in the $O_2$ A band (Xu et al., 2019). Thus, given the advantage of reducing the interference from the surface, the $O_2$ B band is combined with the $O_2$ A band in our algorithm to retrieve aerosol optical central height (AOCH) from TROPOMI (hereafter called the AOCH-$O_2$AB algorithm). Such a combined use provides additional information on the vertical distribution of atmospheric scatterers, attributable to differences in the absorption strengths of the two bands and their underlying surface albedos, as proved by synthetic information content analyses and an application of the SCIAMACHY data (Sanghavi et al., 2012).

Besides the $O_2$ B band, our AOCH-$O_2$AB algorithm also includes the improved representation of aerosol single scattering properties and the assumption of aerosol vertical profile shape (as compared to ALH-$O_2$A). We further showcase the potential application of satellite-retrieved AOCH to improve the estimation of surface PM$_{2.5}$ from the Modern-Era Retrospective analysis for Research and Applications, Version 2 (MERRA-2) dataset. As the first multidecadal reanalysis within which meteorological and aerosol observations are jointly assimilated into a global assimilation system, MERRA-2 provides hourly three-dimensional aerosol concentrations and globally gridded surface PM$_{2.5}$ data. Although bias-corrected AOD from multiple satellite instruments and ground-based observations, such as the Moderate-resolution Imaging Spectroradiometer (MODIS), the Advanced Very High Resolution Radiometer (AVHRR), MISR, and the Aerosol Robotic Network (AERONET), are assimilated in MERRA-2 system, there is no aerosol vertical profile information investigated. This motivates us to apply our retrieved AOD and AOCH-$O_2$AB from TROPOMI into the PM$_{2.5}$ correction of MERRA-2.

We describe the processing of TROPOMI radiances data and ALH-$O_2$AB algorithm development in Section 2. We evaluate the AOCH-$O_2$AB retrievals in Section 3 by focusing on multiple cases of smoke and dust events over dark targets and comparing them with CALIOP aerosol extinction weighted height. An intercomparison with the ALH-$O_2$A product is also conducted in this section. In Section 4, we show the potential application of satellite-retrieved AOD and AOCH to improve
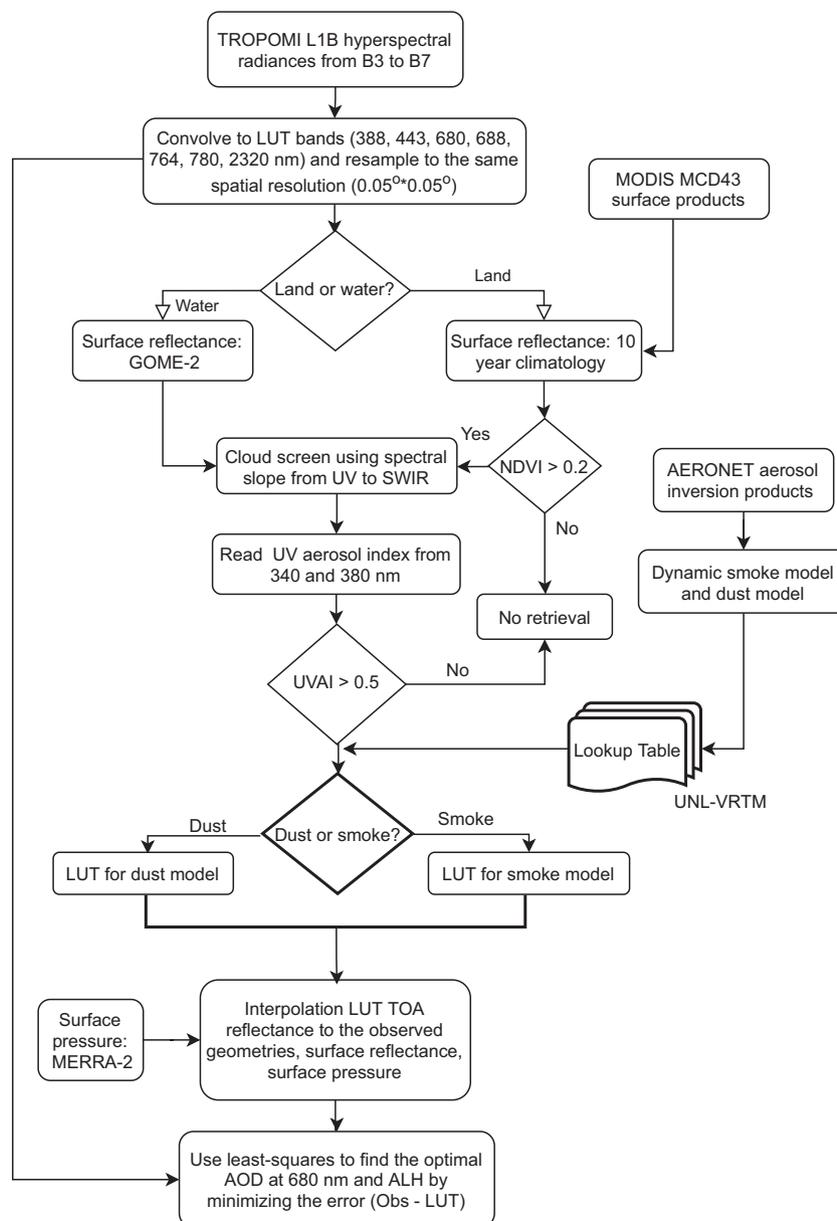


Fig. 1. The flowchart of TROPOMI AOCH retrieval algorithm.

the $PM_{2.5}$ estimates in MERRA-2 based on a smoke event. The conclusions and discussions are given in Section 5.

## 2. ALH retrieval algorithm for TROPOMI

### 2.1. Algorithm overview

Fig. 1 shows the flowchart of the data processing and retrieval steps of the AOCH-$O_2$AB algorithm. These steps are described as follows:

1. Instead of fitting the spectral structure of intensity in each $O_2$ absorption band at high spectral resolution, we use the narrow-band intensities convolved from the TROPOMI hyperspectral level 1B (L1B) measurements ranging from UV to SWIR withassumed spectral response functions for multiple channels. This convolution is used to not only retain the $O_2$ A and B absorption signal in the measurement, but more importantly to improve the retrieval speed using a look-up table (LUT) approach. Otherwise, the retrieval would need to invoke the computationally expensive high-resolution forward radiative transfer simulation to fit the fine spectral structure for gas absorption. Given the coarser spatial resolution of the SWIR spectrometer in comparison to others, we resample the convolved radiance in all narrow bands to the same geolocation grid.
2. The surface reflectance for each pixel is derived after classifying the land and water surface based on the pixel location. We apply different surface reflectance climatology over land and water. For land surface, the normalized difference vegetation index (NDVI) is estimated as well. Considering that the algorithm in this study mainly focuses on dark targets, only those pixels with NDVI >0.2 are used in the following retrieval steps.
3. Cloud-mask procedures are conducted to select cloud-free pixels containing lofted layers of absorbing aerosols that are suitable for ALH retrieval. According to the spectral slope of TOA reflectance between different bands, those pixels contaminated by clouds are screened out. For this study, based on the work of Xu et al. (2019), we mainly focus on retrieval of absorbing aerosols when the UV aerosol index (UVAI) computed at 340 and 380 nm is larger than 0.5.
4. The absorbing aerosol types are classified as either dust or smoke for each valid cloud-free pixel. The aerosol path radiance is approximated and used to distinguish dust and smoke aerosols. Two LUTs calculated with dust or smoke aerosol properties, respectively, will be applied for pixels covered by corresponding aerosol types.
5. The TROPOMI radiance in the $O_2$ A and B bands are compared with the LUT, and the optimal AOD and AOCH are found by minimizing the difference between observations and the LUT. The inversion uses a flexible spectral fitting strategy that multi-band observations could be fitted.

This retrieval procedure has several key differences with that of the AOCH-$O_2$AB algorithm in the literature for EPIC (Xu et al., 2017; Xu et al., 2019). First, the TROPOMI L1B radiance is observed at a high spectral resolution to detect the absorption lines of trace gases, such as ozone or carbon monoxide. However, unlike trace gas retrievals that use the well-defined absorption lines of corresponding trace gases, aerosol retrieval mainly relies on the dependence of aerosol scattering on wavelengths that have no fine spectral structure. Thus, we convolved TROPOMI spectral data with a Gaussian response function to produce narrow-band observations suitable for aerosol retrievals; this step is effectively similar to the OMI UV aerosol retrieval algorithms that use several discrete channels (rather than all channels) (Torres et al., 2007). Second, the cloud screening thresholds of Xu et al. (2019) are based on EPIC visible and near infrared observations, while for this study, we redesign cloud-screening procedures by leveraging the larger spectral range (UV to SWIR) in the TROPOMI measurements. Thus, new thresholds are adopted and a new cloud mask algorithm is developed. Third, we develop a new aerosol type selection method to separate two

types of absorbing aerosols, dust and smoke, based on the approximation of aerosol path radiance in the blue and SWIR bands. Last but not least, the land surface reflectance is updated by averaging MODIS surface products over ten years, and the LUT for smoke and dust properties is updated using the statistical aerosol microphysical parameters from ground-based inversion in recent years. Details about these developments and updates are provided in the following subsections.

### 2.2. Convolving TROPOMI spectra

Operating in low Earth orbit, S5P is designed to have 13:30 local overpassing time as the synergistic exploitation of simultaneous measurements of the Visible Infrared Imaging Radiometer Suite (VIIRS) instrument on-board NASA's Suomi-NPP. In this way, the collocated, high-resolution data from the Visible Infrared Imaging Radiometer Suite (VIIRS) instrument on-board Suomi-NPP could be utilized in TROPOMI data processing. With a 2600 km swath and 16-day orbit repeat period, TROPOMI flies in a sun-synchronous orbit 824 km above the Earth's surface and operates in push broom mode. The S5P trails behind Suomi-NPP by 3.5 min in Local Time Ascending Node, allowing its swath to remain within the scene observed by Suomi-NPP. As a successor of OMI, the TROPOMI combines the strengths of SCIAMACHY, OMI and state-of-the-art technology to provide better performance in terms of sensitivity, spectral resolution and spatial resolution. TROPOMI consists of four spectrometers, each electronically split into two bands, to detect the TOA radiance reflected by the surface in the UV, VIS, near-infrared (NIR), and SWIR, respectively. The spectral and spatial resolutions of the eight bands are (slightly) different. For instance, the spectral resolution is 0.45–0.65 nm for UV or VIS bands, and 0.35 nm for NIR and 0.225 nm for SWIR bands. The footprint of SWIR bands is $5.5 \times 7$ km$^2$, slightly larger than the $5.5 \times 3.5$ km$^2$ of other bands. The wide spectral range of TROPOMI, including the absorption bands of ozone ($O_3$), nitrogen dioxide ($NO_2$), carbon monoxide (CO), sulfur dioxide ($SO_2$), methane ($CH_4$), and formaldehyde ($CH_2O$), provides the ability to monitor these key pollution gases as well as aerosol and cloud properties.

In our retrieval algorithm, the original L1B spectrum with the broad spectral range of each band (30–100 nm) is convolved using narrow-band filters. Then, seven narrow-band radiances at 388, 443, 680, 688, 764, 780, and 2320 nm are derived, respectively. Except for two $O_2$ absorption bands, the radiances in other narrow bands are applied in the cloud mask algorithm. Similar to the "Deep Blue" aerosol retrieval algorithm (Hsu et al., 2006; Hsu et al., 2013), the TOA radiance from the 443 nm band is used for AOD retrieval. At this wavelength, the low surface reflectance for a wide range of surface types, from forested to some arid is helpful for aerosol retrieval. The ratios of the measurements in the $O_2$ A (764 nm) and B (688 nm) bands to their nearby continuum bands at 780 and 680 nm, are intended to be used for deriving AOCH. In addition, similar to the MODIS cloud and aerosol algorithms, the SWIR band (2320 nm) is used for both the cloud mask and absorbing aerosol classification.

Before convolution, based on the quality flags defined in L1B data, only those pixels with good quality at each sampling wavelength are selected for the subsequent spectral convolution. In the convolution process, we apply the spectral response function of EPIC in corresponding bands as the convolution filters. For those bands not involved in EPIC (e.g., 2320 nm), a Gaussian response function with a fixed full width at half maximum (FWHM) (2.355 nm, standard deviation of Gaussian distribution is 1 nm) is used instead. Fig. 2 provides all of the narrow-band filters we used along with atmospheric transmittance across the entire TROPOMI spectral range. The filters in the $O_2$ A and $O_2$ B bands are compared with the standard TROPOMI response functions with fine FWHM (0.35 nm, the spectral resolution we mentioned above, from L1B data) in Fig. 2b and c, respectively. It is found that the (EPIC) narrow-band filters with coarser FWHM still catch the $O_2$ absorption by giving more weight to the spectral response at the main $O_2$ absorption
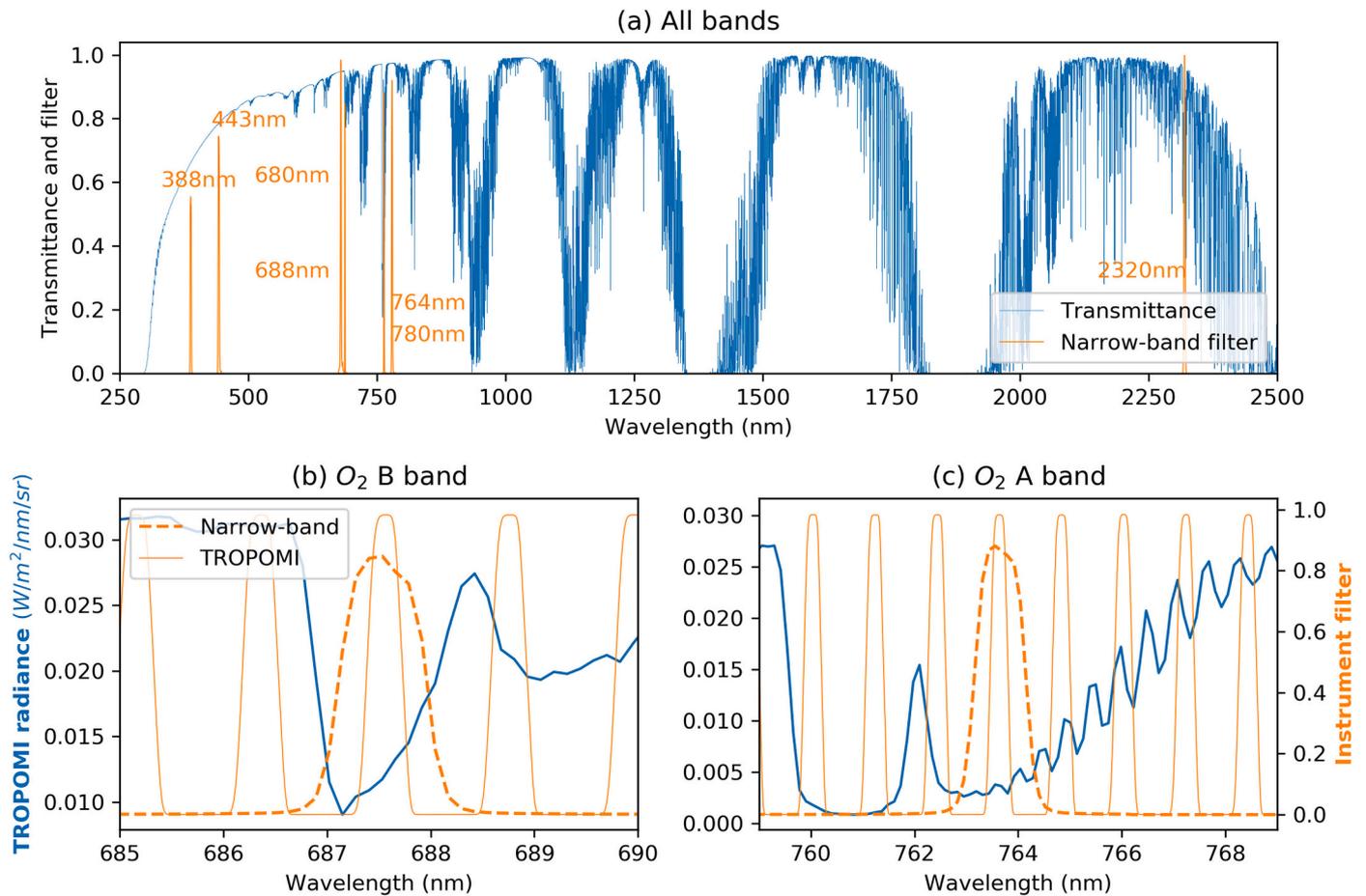
**Fig. 2.** The narrow-band filters used in this study to convolve TROPOMI spectra with high resolution: (a) the filters in all seven bands we use and the transmittance; (b) comparison of the narrow-band filter and the high-resolution standard filter in TROPOMI L1B data in the $O_2$ B band expressed as "Narrow-band" and "TROPOMI" here; (c) is the same as (b) but for the $O_2$ A band.

lines. Ultimately, the convolved narrow-band TROPOMI-observed TOA radiances could be converted to TOA reflectance similar to LUT from radiative transfer simulation following the definition in Eq. (1):

$$\rho = \frac{\pi I}{cos\theta_0 E_0},\qquad(1)$$

where $\rho$ and $I$ represent the TOA reflectance and TOA radiance, respectively, $E_0$ denotes the incoming solar irradiance, and $\theta_0$ is solar zenith angle. In this study, the daily observed TROPOMI solar irradiance data is used (https://sentinels.copernicus.eu/documents/247904/3541451/Sentinel-5P-Level-1b-Product-Readme-File).

There are several reasons to use narrow-band instead of original hyperspectral observations for aerosol retrievals. First, even though the information content of aerosol profiles increases as the spectral resolution of measurements increases, the signal-to-noise ratio (SNR) decreases owing to less signal detected in each channel at finer resolution. The coarser resolution of the narrow-band filter (dashed orange line in Fig. 2b) contributes higher SNR than the TROPOMI spectral response function (solid orange line in Fig. 2b). Based on the spectral resolution of TROPOMI, fewer than two pieces of information about AOCH are contained in a single $O_2$ absorption channel (Colosimo et al., 2016; Frankenberg et al., 2012; Geddes and Bösch, 2015). Therefore, the convolution can reduce the influence of low SNR but still maintain a similar level of ALH information content. Second, unlike trace gases whose absorption lines determine the fine structure of the spectrum, the aerosol properties are retrieved in accordance with the variation of aerosol scattering within a large range of wavelengths well constrained by multi-channel observations from UV to NIR. For instance, the OMI

aerosol retrieval algorithm fits narrow-band radiance in several atmospheric window channels rather than a fine spectral structure (Torres et al., 2007). Last but not least, fitting the fine spectral structure of observations consumes far more time, resulting in unacceptable computational burden for an operational algorithm producing near-real-time products; this high computational demand is one of the motivations to use the neural network (NN)-based forward model in the current TROPOMI ALH operational algorithm (Nanda et al., 2019). In contrast, fitting narrow-band measurements through look-up tables, as done in several aerosol retrieval algorithms, is computationally efficient and fast.

After convolution, due to the coarser spatial resolution in the SWIR (2320 nm band) than the other narrow bands, the TOA reflectance in all narrow bands are resampled into the same 0.05° × 0.05° standard grids based on the geolocation information. These standard-grid measurements (hereafter called TROPOMI narrow-band measurements) are used in the following steps.

### 2.3. Masking cloudy pixels

After acquiring TROPOMI narrow-band TOA reflectance, the algorithm conducts a series of steps to select cloud-free pixels suitable for aerosol retrieval. Even though the cloud product from VIIRS/Suomi-NPP can be co-located to mask out TROPOMI cloudy pixels (in a manner that is adopted in the TROPOMI ALH-$O_2$A algorithm and provided as an S5P-NPP auxiliary cloud product by TROPOMI), VIIRS data needs to be resampled to the TROPOMI footprint, leading to uncertainty due to spatial and temporal mismatch. Here we utilize an independent cloud

mask method that uses solely TROPOMI data, which compensates for the lack of near-real-time cloud mask and is regarded as a candidate for application in the operational algorithm in the future.

Fig. 3a, c, and e show a cloud screening example for a smoke case over vegetation. Based on the VIIRS true color image (with observation time in close proximity to TROPOMI), the four regions indicated by red boxes are selected to represent (1) a clear-sky vegetation region without aerosols (vegetation); (2) a cloud-free thick smoke region (smoke1); (3) a cloud-free thin smoke region (smoke2); and (4) a cloudy region (cloud), respectively (Fig. 3a). By averaging TROPOMI TOA reflectance at all pixels in each region box, their mean values at all narrow bands except the $O_2$ absorption bands are compared (Fig. 3c). It is clear that not only is the TOA reflectance for cloudy pixels in all bands higher than those for cloud-free pixels, but the reflectance wavelength dependence also shows an obviously distinction, especially in the VIS and NIR (or SWIR) bands, similar to the findings in our previous study (Xu et al., 2018b). Based on this principle, different spectral slopes of TOA reflectance between bands from UV to SWIR, expressed as Eq. (2), are

used as the criteria to classify a pixel as cloudy:

$$k_{\lambda_1, \lambda_2} = \frac{|\rho_{\lambda_1} - \rho_{\lambda_2}|}{\lambda_2 - \lambda_1}, (\lambda_1 < \lambda_2) \qquad (2)$$

Here, $\rho_{\lambda_1}$ (or $\rho_{\lambda_2}$) represents the TOA reflectance at $\lambda_1$ (or $\lambda_2$) wavelength. It must be mentioned that the thick aerosol plumes sometimes show characteristics close to those of cloudy pixels (smoke1 in Fig. 3c), while the thin smoke shows a curve similar to clear-sky pixels without smoke (smoke2 in Fig. 3c). Therefore, the key challenge in our cloud-masking process is to screen out cloudy pixels while keeping pixels covered by thick aerosol layers. For this purpose, we define the ratio between two slopes as the criteria rather than $k_{\lambda_1, \lambda_2}$ themselves. According to Fig. 3c, not only is $k_{780, 2320}$ higher for cloudy pixels than for cloud-free pixels, but also is the ratio of $k_{680,780}$ to $k_{780, 2320}$ is also much lower in cloudy regions than in other regions. As a result, both the spectral slopes themselves and the ratio between the two spectral slopes are used to mask cloudy pixels. Besides these special spectral slope tests, TOA reflectance tests and spatial homogeneity tests similar to those used
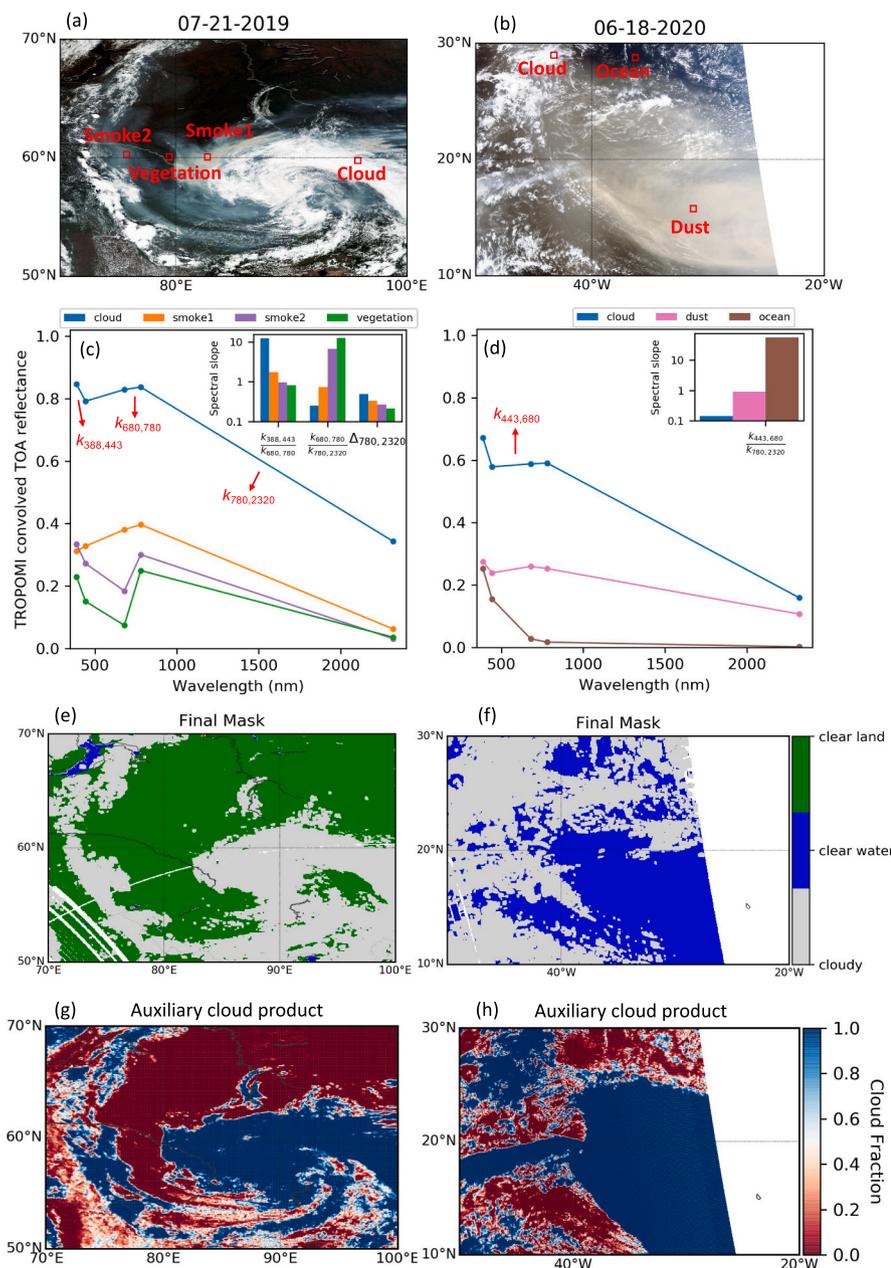


**Fig. 3.** True color images from VIIRS/Suomi-NPP (a and b), spectral signal analysis of different pixel types (c and d), the final mask map of clouds, clear land, and clear water (e and f) based on the thresholds for all tests in Table 1, and the cloud fraction from the corresponding S5P-NPP auxiliary cloud product (g and h) in smoke and dust events primarily over vegetated (21 July 2019, left column) and ocean surfaces (18 June 2020, right column), respectively. The spectral analysis in (c) and (d) shows the variation of the convolved narrow-band TROPOMI TOA reflectance as a function of their central wavelengths for those pixels marked by the red boxes in panels (a) and (b), respectively, corresponding to being covered by clouds and thin and thick aerosol plumes over land or ocean. The smaller panels in (c and d) indicates the values of four types of pixels for three (or one in d) spectral slope tests. Each spectral slope is defined by the dot line shown by the red arrow. The white spaces in panels (e) and (f) indicate there are no valid TROPOMI measurements over these pixels. (For interpretation of the references to color in this figure legend, the reader is referred to the web version of this article.)

by Martins et al. (2002) and Xu et al. (2017) are used in this study as well. In addition, because the surface reflectance of water and land show different wavelength dependence (compare Fig. 3c and d), the spectral slopes between different bands are used in the cloud mask, and the definition of the threshold of each test also depends on surface type. Finally, the threshold defined for each test used to screen out cloudy pixels is summarized in Table 1 for land and water, respectively. Three thresholds of $\rho_{443}$, $\rho_{680}$, and $\rho_{780}$ are applied for both land and water, as well as the standard deviation of $\rho_{388}$ within $3 \times 3$ adjacent pixels, chosen as a homogeneity test. But in spectral slope tests, three slope ratios and one slope ($\Delta_{780, 2320}$) are used for land, while only $\frac{k_{443,680}}{k_{780,2320}}$ is applied over water. Similarly, the $\rho_{2320}$ threshold is only used over land and not water. All the thresholds in Table 1 are defined based on multiple tests for different smoke and dust events over ocean and land. However, given the limited case studies, these cloud mask tests may still have unexpected weaknesses when applying globally. Thus, more tests should be done by fully exploiting the spectral slopes from UV to SWIR enabled uniquely by TROPOMI for cloud screening before applying it globally in the operational algorithm. Furthermore, these thresholds are only defined for dark surfaces including water and vegetated surfaces; they must be adjusted for bright surfaces due to the different wavelength dependence of surface reflectance, which will be studied in the future. As a result, as shown in the flowchart in Fig. 1, we use NDVI derived from the MODIS surface product (details are provided in Section 2.5) as the criteria to screen out bright surfaces (NDVI $\leq$ 0.2) that are not suitable for this retrieval algorithm before cloud masking over land.

Based on the thresholds in Table 1, the final cloud mask results for two examples (Fig. 3a and b) are illustrated in Fig. 3e and f. We compare them with the cloud fraction from the S5P-NPP auxiliary cloud product (Fig. 3g and h), which provides a statistical summary of the NPP-VIIRS level 2 Cloud Mask (VCM) in each S5P field of view (FOV). The cloud fraction is calculated as the ratio of the number of VIIRS pixels classified as "probably cloudy" and "confidently cloudy" to the total number of VIIRS pixels in the TROPOMI nominal footprint. It is clear that our cloud mask has better performance in those pixels covered by thick aerosol plumes, which are always misclassified as cloudy pixels with high cloud fraction (close to 1.0) in VCM; see the dust scene in Fig. 3h. Generally, the cloud mask method combining TOA reflectance spectral slope tests with reflectance and homogeneity tests in this study not only classifies the cloudy pixels with good performance but is also useful in TROPOMI near-real-time retrieval as an independent process that does not rely on a VIIRS product.

## 2.4. Aerosol type classification

As two major types of absorbing aerosols, coarse dominated dust particles and fine dominated smoke particles must be differentiated before fitting measured reflectance to LUT reflectance in the algorithm. First, after screening out cloudy pixels, only the remaining pixels with UVAI between 340 and 380 nm from TROPOMI operational level 2 aerosol index product larger than 0.5 are identified as absorbing aerosols suitable for retrieval. Secondly, we classify the aerosols in these

pixels as smoke or dust based on their differences in spectral scattering that arise from their respective sizes.

Dust particles are more than an order of magnitude larger in size than smoke aerosols (e.g. volume median diameter of 5 μm versus 0.3 μm), leading in part to their stronger scattering at longer wavelengths, such as SWIR or infrared channels (Carboni et al., 2007; Skiles et al., 2017; Wang et al., 2010). This distinct characteristic of dust particles results in stronger path radiance in SWIR where the path radiance of small particles is weak and can be ignored (Hou et al., 2017). In early studies of the theoretical basis for the operational MODIS retrieval algorithm (Kaufman et al., 1997), a ratio of aerosol single-scattering path radiance ($L_\lambda$*, $\lambda$ is the wavelength) in the red and blue channels was used to determine the aerosol model. By defining thresholds of this ratio, dust and non-dust aerosols can be distinguished. $L_\lambda$* is defined as Eq. (3):

$$L_\lambda^* = \tau_\lambda P_\lambda \omega_\lambda, \tag{3}$$

where $\tau_\lambda$, $P_\lambda$ and $\omega_\lambda$ represent the aerosol optical depth, scattering phase function, and single scattering albedo (SSA) at wavelength $\lambda$, respectively. $L_\lambda$* can be calculated by using the prescribed optical properties of dust and smoke particles, as well as the satellite measurements following Eq. (4):

$$\rho(\theta, \theta_0, \varphi) = \frac{\rho_m(\theta, \theta_0, \varphi) + L^*(\theta, \theta_0, \varphi) + F_0(\theta_0)T(\theta)\rho_s(\theta, \theta_0, \varphi)}{1 - s\rho'}. \tag{4}$$

Here, $\theta$ and $\varphi$ are the viewing zenith angle and relative azimuth angle. $F_0(\theta_0)$ represents the normalized downward solar flux, and $T(\theta)$ is the transmission into the direction of satellite view. $s$ is the atmospheric backscattering ratio, and $\rho'$ represents the surface reflectance averaged over viewing and illumination angles, while $\rho_s(\theta, \theta_0, \varphi)$ is the bidirectional surface reflectance. $\rho_m(\theta, \theta_0, \varphi)$ and $L^*(\theta, \theta_0, \varphi)$ are the path radiance due to molecular scattering and aerosol scattering, respectively. Following the study in Kaufman et al. (1997), the difference ($L_\lambda$) between surface reflectance and TOA reflectance (i.e., $L_\lambda = \rho_{s, \lambda} - \rho_\lambda$) describes the atmospheric path radiance including molecular and aerosol scattering at wavelength $\lambda$ if we simplify the surface reflectance as a Lambertian albedo. For different aerosol types at the same wavelength, the molecular scattering is assumed to be consistent, hence the variable $L_\lambda$ only depends on aerosol path radiance. According to the simulations in Hou et al. (2017), for vegetated surfaces at shorter wavelengths, such as the blue band, $L_\lambda$ is negative regardless of aerosol particle size. In contrast, in SWIR, the weak path radiance of fine particles has little impact on TOA radiance, resulting in positive $L_{2320}$ or small negative values; meanwhile, $L_{2320}$ for coarse aerosol particles always shows large negative values. Therefore, the ratio $L_{2320}/L_{443}$ (hereafter called the path radiance ratio) is used here as a criterion to classify large dust particles and small smoke particles. This rationale is similar to the definition of nondust absorbing aerosol index in the previous study about MODIS data (Ciren and Kondragunta, 2014). In addition, even though the absorptions at wavelength close to 2320 nm by carbon monoxide (CO) and methane (CH$_4$) (likely associated with smoke plume) can lower $\rho_{2320}$ compared to normal conditions (i.e., without CO and CH$_4$), these gases are unlikely to be associated with dust plume,

**Table 1**
The thresholds of all tests used in cloud mask for two types of surface: land and water.

| Band (nm) | Reflectance tests | | | | Spectral slope tests | | | | Spatial homogeneity tests |
|---|---|---|---|---|---|---|---|---|---|
| | 443 | 680 | 780 | 2320 | $\dfrac{k_{388,443}}{k_{680,780}}$ | $\dfrac{k_{680,780}}{k_{780,2320}}$ | $\dfrac{k_{443,680}}{k_{780,2320}}$ | $\Delta_{780, 2320}$[d] | 388 |
| Land[a] | 0.45 | 0.5 | 0.5 | 0.15/0.35[b] | 7.0 | 0.25 | – | 0.4 | 0.015 |
| Water | 0.4 | 0.5 | 0.5 | –[c] | – | – | 0.5 | – | 0.005 |

[a] Here, only vegetated surfaces are considered, not bright surfaces.
[b] The value to the left of "/" indicates the threshold for NDVI $\geq$ 0.6, while the value to the right is for 0.2 < NDVI <0.6 due to the large dependence of TOA reflectance in SWIR on the surface.
[c] "–" represents that the test is not used.
[d] To keep all thresholds at a similar order of magnitude, we define $\Delta_{780, 2320} = | \rho_{780} - \rho_{2320}|$ here.

resulting in positive $L_{2320}$ like fine smoke particles. Therefore, the gas absorption has little impact on the absorbing aerosol classification.

To test the aforementioned method, several small regions covered by dust or smoke aerosols with different AOD or surface reflectance scenarios were selected based on VIIRS true color images of several cases. In each region, the path radiance ratio is estimated from TROPOMI narrow-band TOA reflectance and real surface reflectance from an ancillary satellite product (e.g., MODIS or Global Ozone Monitoring Experiment-2, GOME-2, as described later in Section 2.5) at each pixel. Considering the different TROPOMI observation geometries for different pixels, the path radiance ratios are shown as a function of the scattering angle in Fig. 4. Similarly, the impact of AOD and surface reflectance on the path radiance ratio is tested (differently colored dots). It is clear that in dust cases, $L_{2320}/L_{443}$ are always positive and larger than those for smoke cases despite different surface reflectance and AOD; meanwhile, $L_{2320}/L_{443}$ has little dependence on the scattering angle. As a result, a threshold could be defined to determine whether a cloud-free pixel has dust or smoke particles, and hereafter, corresponding LUT is used in the retrieval. Fig. 5 shows the application of this path radiance ratio threshold (0.15) in the aerosol type classification for one case over the Tropical Atlantic Ocean on 15 February 2020. In this region, the dust plumes coming from the Sahara Desert may be transported southward over ocean and meet the smoke plume generated by the wildfires over land in tropical Africa along the coastal region; thus, the dust and smoke classification is significant in the retrieval when both aerosols may exist. According to the path radiance ratio $L_{2320}/L_{443}$ (Fig. 5c), the southwestern part of the aerosol plume, where $L_{2320}/L_{443}$ is larger than 0.15, is classified as dust transported from the desert to the ocean, while the eastern part is classified as smoke plume from the fires burning on northeastern land ($L_{2320}/L_{443} < 0.15$). The threshold defined here is based on several case studies over dark targets, and it deserves more consideration; tests should be applied globally in the future. To compare with our classification results using the path radiance ratio threshold (Fig. 5d), the Angstrom Exponent retrieval from the VIIRS Deep Blue aerosol product for the example granule is presented in Fig. 5e. The large Angstrom Exponent ($> 2.0$) from VIIRS confirms the smoke pixels in

Fig. 5d showing small particle size, while dust pixels with large particles have a smaller Angstrom Exponent ($< 0.7$). However, the mixed aerosols are still difficult to be distinguished in this method and may be misclassified as smoke along the coast in Fig. 5d. The classification of mixed absorbing aerosols deserves more research in the future; in this study, we mainly focus on dust-dominated and smoke-dominated absorbing aerosols. The VIIRS product provides a reference for the reliability and feasibility of our classification method even though it has uncertainty. Although the depolarization ratio of CALIOP provides more reliable information about non-spherical dust particles, it is hard to compare different aerosol subtypes at multiple layers from lidar with only one type from passive sensors at each pixel. Moreover, the CALIOP classification of fine and mixed absorbing aerosols is not as good as coarse absorbing aerosols after being validated by AERONET inversions and still have some issues in the coastal region (Ciren and Kondragunta, 2014; Ford and Heald, 2012; Schuster et al., 2012; Yang et al., 2013). Generally, our classification method for dust and smoke particles will be validated and improved in the future and deserves an independent study.

### 2.5. Look-up tables and surface reflectance

Following previous studies (Xu et al., 2017; Xu et al., 2019), an LUT is generated in which narrow-band TOA reflectances at 443, 680, 688, 764, and 780 nm are precomputed from the Unified Linearized Vector Radiative Transfer Model (UNL-VRTM) for a set of AOD and AOCH values under multiple atmospheric and observation scenarios described by different surface reflectance values, Sun-Earth-satellite viewing geometries and surface pressures. Considering the limited number of aerosol layers information from $O_2$ absorption measurements with moderately high spectral resolution (0.4 nm like SCIAMACHY and TROPOMI) (Corradini and Cervino, 2006), in the simulation, the aerosol profile is assumed to follow a quasi-Gaussian distribution function as in Eq. (5):
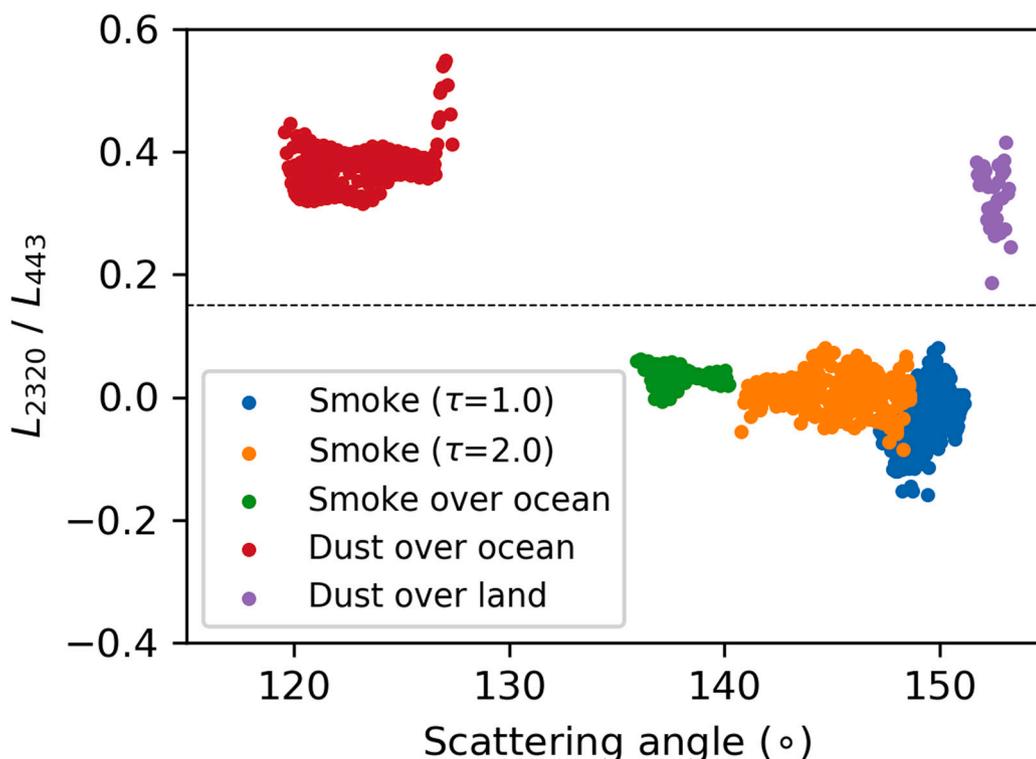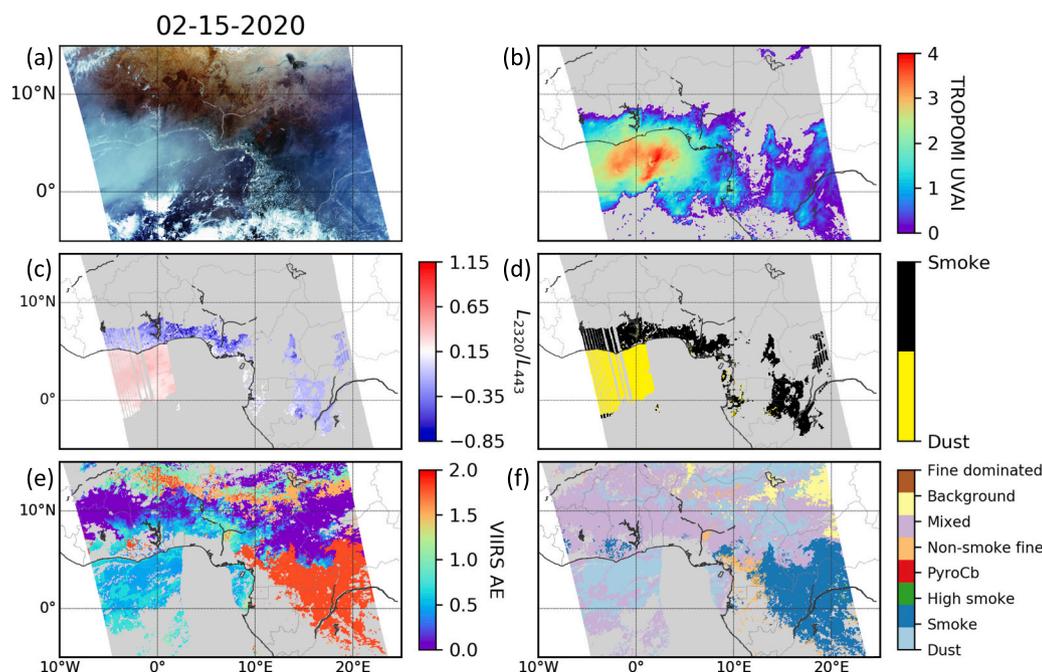


**Fig. 4.** The path radiance ratio $L_{2320}/L_{443}$ calculated from real TROPOMI data and surface reflectance data (from the MODIS MCD43 product introduced in Section 2.5) at all pixels in five different regions as the function of the scattering angle. The five regions, including the smoke over land with 1.0 and 2.0 AOD, smoke over ocean, dust over ocean and land cases, are represented by differently colored dots. Here, the AOD of the smoke case is derived based on MODIS AOD retrieval. The scattering angle is calculated from TROPOMI L1B geometry data at each pixel.

**Fig. 5.** Dust and smoke classification according to the path radiance ratio $L_{2320}/L_{443}$ (c) calculated from TROPOMI TOA observations and surface reflectance data for the aerosol plume over the North Atlantic Ocean on 15 February 2020. Panel (a) shows the true color image from VIIRS and (b) illustrates the UVAI between 340 and 380 nm from TROPOMI Level 2 aerosol index product. Panel (d) shows the final classification result for each pixel suitable for retrieval. The pixels with sun glint angle less than 30° are excluded in (c) and (d). The Angstrom Exponent and aerosol type retrieval in this region from VIIRS level 2 Deep Blue aerosol product are shown in (e) and (f). (For interpretation of the references to color in this figure legend, the reader is referred to the web version of this article.)

$$\tau(z) = c \frac{exp(-\sigma|z - \text{AOCH}|)}{[1 + exp(-\sigma|z - \text{AOCH}|)]^2}, \quad (5)$$

where $\tau(z)$ represents the aerosol extinction coefficient at height $z$. According to $\text{AOD} = \int_0^{TOA} \tau(z)dz$, $c$ is a constant derived from AOD. As a result, the shape of aerosol extinction vertical distribution depends on two parameters: a half-width related parameter $\sigma$ and AOCH. Based on Eq. (5), when $z = \text{AOCH}$, $exp(-\sigma|z - \text{AOCH}|) = 1$, so $\tau(z)$ reaches a maximum. In other words, AOCH is the height where aerosol extinction is the largest. As in our previous studies, $\sigma$ is fixed as 1.76 km (corresponding to 1.0 km half-width) in the simulations and only AOCH and AOD will be retrieved.

In this retrieval algorithm, two LUTs simulated with different aerosol optical properties representing dust and smoke aerosols are implemented. The dust aerosol model follows Xu et al. (2017) considering the particle non-sphericity, while the smoke aerosol model in Xu et al. (2019) is updated in this study using the AERONET inversion products located in North America in the summer of 2018 and 2019. The smoke microphysical parameters including the effective radius ($r_{eff}$) and variance ($v_{eff}$) for fine and coarse modes in bi-lognormal particle size distribution, the volume fine mode fraction ($fmf_v$), and the wavelength dependent refractive index (real part $m_r$ and imaginary part $m_i$), are derived from AERONET inversion products when the UVAI of TROPOMI is large ($\geq 1.0$). Statistically, the AERONET data two hours before and after TROPOMI overpass time are used to drive the climatological microphysical parameters of smoke (Table 2), including $m_r$ and $m_i$ at all five wavelengths, $r_{eff}$ and $v_{eff}$ for two aerosol modes, and $fmf_v$. Among these parameters, the $r_{eff}$ for fine and coarse modes, $fmf_v$, $m_r$ at 680 and 780 nm are assumed to increase linearly when AOD increases, while others are independent of AOD. Here, the refractive index at 780 nm is interpolated by AERONET inversion products at 675 nm and 870 nm.

We also assume that the refractive index at the $O_2$ absorption band is the same as its nearby continuum band, i.e., $m_r$ and $m_i$ at 688 nm are the same as 680 nm. Applying these microphysical parameters in the Lorenz-Mie theory based on the spherical assumption of smoke particles, the single scattering properties of smoke are calculated and input into the radiative transfer simulation. Compared with the other smoke optical model in the literature, the SSA of this updated model is higher (0.95–0.96) and closer to the ground-based observation for smoke cases in North America in recent years. For the dust model, we continue using the climatological phase function, SSA and Angstrom Exponent between 440 nm and 870 nm from the AERONET inversion product considering non-spherical dust particles at sites close to the Sahara Desert (Fig. 6). As illustrated by Xu et al. (2017), only the AERONET inversions with $fmf_v < 0.4$ and $\text{AOD}_{440} > 0.4$ are identified as dusty scene and involved in the statistics. Consequently, neither the Mie nor the T-matrix model is used in the dust LUT simulation. Except for the aerosol properties, the spectral settings and other scenario parameters in the LUT are defined as in Xu et al. (2019).

The surface reflectance database is used as ancillary information in the retrieval algorithm. Similar to previous studies (Xu et al., 2017; Xu et al., 2019), based on the Global Self-consistent, Hierarchical, High-resolution Geography Database (GSHHGD) (Wessel and Smith, 1996), each TROPOMI pixel is classified as either land or water according to its location. Over water, the GOME-2 surface Lambert-equivalent reflectivity (LER) database is applied, and the MODIS BRDF/Albedo product (MCD43) is used for land pixels. Instead of using the 16-day averaged MODIS product for the retrieval date, a climatological surface reflectance database based on ten years of MODIS is used to reduce the uncertainty of atmospheric correction in the surface product. The surface reflectance in MODIS's seven bands and GOME-2's 12 bands are fitted to the TROPOMI narrow bands by the linear regression method from USGS

**Table 2**

The climatological microphysical parameters for smoke aerosols from AERONET inversion products in North America in the summers of 2018 and 2019.
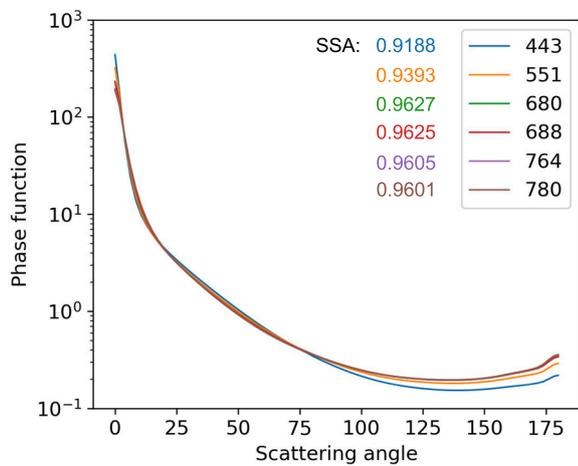
| Microphysical parameters | $r_{eff}$ | $v_{eff}$ | $fmf_v$ | $m_r$ (443 nm) | $m_i$ (443 nm) | $m_r$ (680 nm) [b] | $m_i$ (680 nm) [b] | $m_r$ (780 nm) [b] | $m_i$ (780 nm) [b] |
|---|---|---|---|---|---|---|---|---|---|
| Fine mode | $0.017\tau+0.178$ [a] | 1.26 | $0.162\tau+0.532$ | 1.54 | 0.0106 | $0.026\tau+1.513$ | 0.00857 | $0.025\tau+1.513$ | 0.00855 |
| Coarse mode | $0.579\tau+2.477$ | 0.278 | | | | | | | |

[a] $\tau$ is the AOD at 680 nm.

[b] The $m_r$ and $m_i$ at 688 nm are the same as 680 nm. Similarly, the $m_r$ and $m_i$ at 764 nm are the same as 780 nm.

**Fig. 6.** The climatological phase function and SSA for dust events from AER-ONET inversion products at sites close to the Sahara Desert. Different colors correspond to different channels.

reflectance spectra data (Kokaly et al., 2017), as described by Xu et al. (2019). This study still focuses on retrieval at dark targets, including vegetation land surface and water surface, while those pixels with bright surface are screened out by NDVI $\leq$ 0.2 over land.

According to the flexible spectral fitting method introduced by Xu et al. (2019), the AOD is determined by matching the TROPOMI narrow-band TOA reflectance at 443 nm with the LUT. Next, this estimated AOD is applied in fitting the DOAS ratios (defined as the ratio of TOA reflectance between the absorption band and the continuum band) of the $O_2$ A and B bands to find the optimal AOCH minimizing the square error between observation and LUT (least-square method). In the DOAS ratios fitting process, the weights of the $O_2$ A and B bands are used and change with surface type. For vegetated surface, the weight of the $O_2$ B band is set as 0.7–0.9, larger than the $O_2$ A band (corresponding 0.3–0.1) due to its lower surface reflectance, which is beneficial for aerosol retrieval.

## 3. Retrieval case studies and validation

After applying our two-band retrieval algorithm in several smoke and dust events, we present details of our AOCH-$O_2$AB retrievals for seven cases (Section 3.1) and compare them with TROPOMI operational ALH-$O_2$A products. Furthermore, the AOCH-$O_2$AB and ALH-$O_2$A are also compared with satellite lidar CALIOP backscatter (532 nm) and aerosol extinction (532 and 1064 nm) profile products. Lidar profiles from CALIOP provides the accurate and reliable detailed vertical structure of the aerosols, and therefore can be regarded as the benchmark for validating passive ALH remote sensing. The CALIOP level 1B backscatter profiles are compared with two products visually and their performance is quantified by the level 2 aerosol extinction profiles. In addition, our retrieved AOD is validated by the ground-based AERONET AOD in Section 3.2 as well.

### 3.1. AOCH retrievals and comparison

Fig. 7 displays our AOCH-$O_2$AB retrieval for five selected smoke cases and two dust cases (seven rows) . The true color images from VIIRS/Suomi-NPP for each case are shown in the first column in Fig. 7, in which the CALIOP ground tracks are shown as red lines. AOCH-$O_2$AB retrieved from our algorithm in the second column is compared with ALH-$O_2$A (the third column) from the TROPOMI operational retrieval algorithm using only one $O_2$ absorption band. The right column compares the collocated AOCH-$O_2$AB and ALH-$O_2$A with CALIOP level 1B total attenuated backscatter at 532 nm (curtain plots). It should be
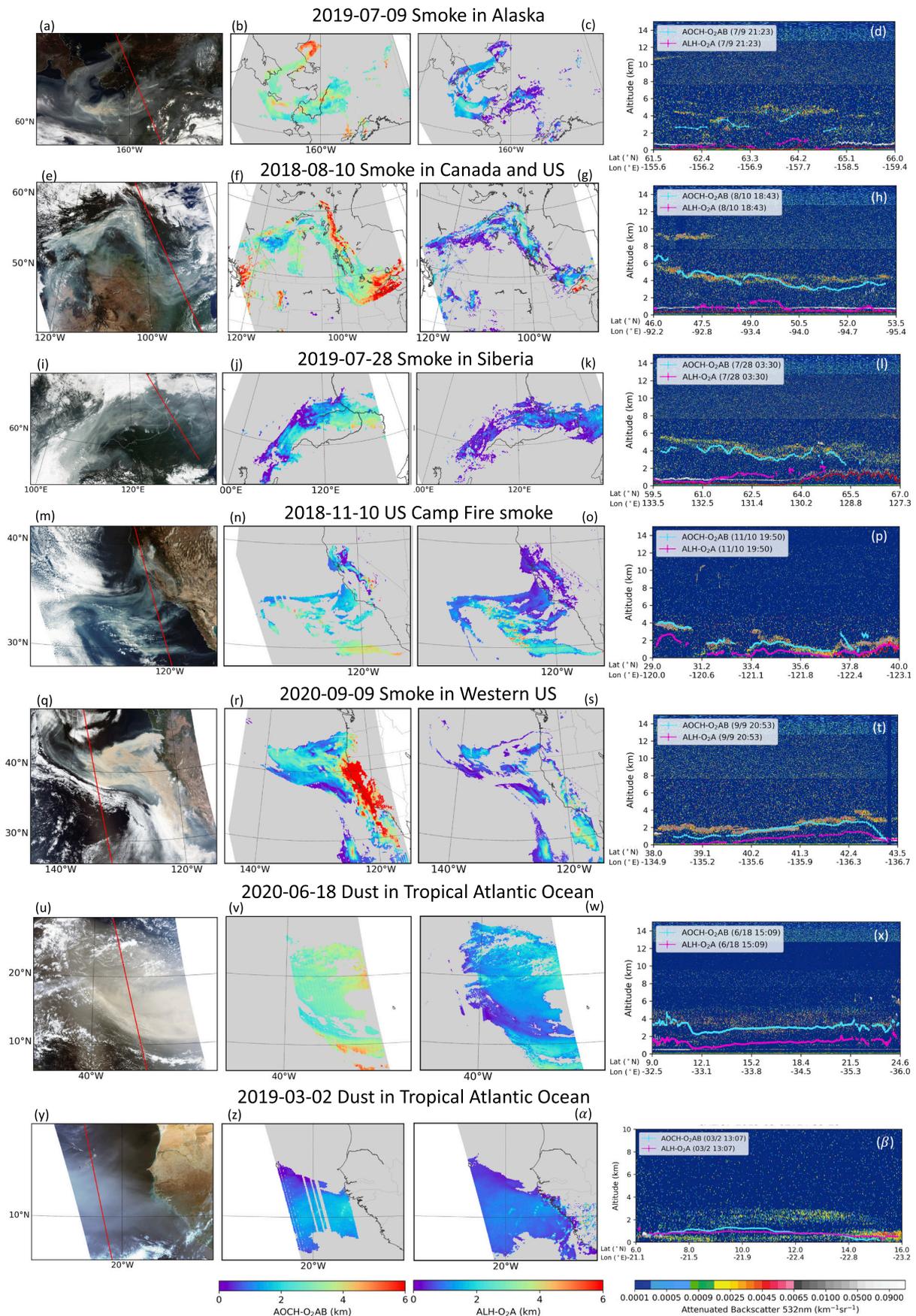
mentioned that our AOCH-$O_2$AB retrieval represents the AOCH above the surface, while the ALH-$O_2$A products indicates the middle height of the aerosol layer relative to the geoid (http://www.tropomi.eu/sites/def ault/files/files/publicSentinel-5P-Aerosol-Layer-Height-Product-Read me-File.pdf), so we transfer the ALH-$O_2$A to a height relative to the surface for comparison, as shown in the third column of Fig. 7. When compared with CALIOP profiles (in the last column of Figs. 7 and 8), the AOCH-$O_2$AB is adjusted by the surface elevation from CALIOP products and represents the height relative to mean sea level, which is consistent withCALIOP altitude and ALH-$O_2$A.

The first three cases (2019-07-09, 2018-08-10, 2019-07-28) are smoke events over vegetation in different regions around the world. On 9 July 2019, after the fires had been burning for two days, a big smoke plume was generated that covered the whole Alaskan region in the US. AOCH-$O_2$AB values from our retrieval algorithm for this plume are found to be 2–5 km, while ALH-$O_2$A values are nearly exclusively below 3 km at all retrieval pixels. AOCH-$O_2$AB for the north part of the plume can reach 5–6 km, higher than that of other parts of the plume (around 3 km). However, ALH-$O_2$A indicates greater aerosol heights at the southwest of the plume (3 km), while in other areas the plume is located almost entirely in the boundary layer. Clearly, the two products show different spatial patterns for the smoke plume vertical distribution. When compared with ALH-$O_2$A (below 1 km), AOCH-$O_2$AB is closer to the CALIOP height with dominant backscatter signal of CALIOP (3–4 km, Fig. 7d).

Similar performance is found for the smoke plume on 10 August 2018 in the central US and Canada; AOCH-$O_2$AB values of 3–4 km are greater than ALH-$O_2$A and closer to CALIOP height with strong back-scatter (Fig. 7, 2nd row). Unlike the 9 July 2019 case, the spatial patterns of AOCH-$O_2$AB and ALH-$O_2$A are similar for this smoke plume. For a smoke event on 28 July 2019 over Siberia (Fig. 7, 3rd row), AOCH-$O_2$AB values are below 4 km for all retrieval pixels and lower than the first two cases, indicating the different vertical structures of this smoke plume. ALH-$O_2$A values for this case are all still below 3 km, and are not as close to CALIOP backscatter as AOCH-$O_2$AB. In addition to the east part of this smoke plume where ALH-$O_2$A values are ~3 km, ALH-$O_2$A values are always lower in other regions. In contrast, not only in the east part, but also in the south of this plume, AOCH-$O_2$AB values are higher (3–4 km). In other words, AOCH-$O_2$AB captures the spatial trend of smoke plume height but ALH-$O_2$A may miss, which will affect the study of smoke plume structure and physics.

The fourth and fifth cases (2018-11-10 and 2020-09-09, Fig. 7, 4th and 5th rows) illustrate the retrievals for fires starting along the US west coast and smoke plumes that were subsequently transported to the ocean, respectively. For the Camp Fire smoke plume on 10 November 2018, higher values of AOCH-$O_2$AB (3–4 km) are found for the down-wind region in the south of the plume, while aerosols layer at the fire source region in the north are in the lower atmosphere. ALH-$O_2$A shows spatial patterns similar to those of AOCH-$O_2$AB but is biased 1–2 km low when compared with both AOCH-$O_2$AB and the altitude with the strongest CALIOP backscatter. In addition, ALH-$O_2$A retrieval still contains several pixels contaminated by scattered clouds, which were screened out clearly in our AOCH-$O_2$AB retrieval. Similarly, ALH-$O_2$A values of California Fire smoke on 9 September 2020 are also smaller than AOCH-$O_2$AB and CALIOP data but present spatial distribution similar to AOCH-$O_2$AB. For this thick smoke plume, our AOCH-$O_2$AB retrieval captures the plume with better coverage including the high smoke altitude along the coastline (Fig. 7r), while ALH-$O_2$A misses those plume pixels misclassified as clouds by VIIRS cloud mask (Fig. 7s).

The last two examined cases were for dust plumes over the tropical Atlantic Ocean originating from the Sahara Desert in the spring and summer (2019-03-02 and 2020-06-18). On 18 June 2020, the dust plume was transported a long distance, and could be lifted to 2–5 km as shown by CALIOP backscatter (Fig. 7x). The retrieved AOCH-$O_2$AB ex-hibits the comparable plume height, but ALH-$O_2$A yields a dust layer 2 km lower, despite the similar spatial patterns between these two (Fig. 7v

(a) (b) (c) (d)
2019-07-09 Smoke in Alaska

(e) (f) (g) (h)
2018-08-10 Smoke in Canada and US

(i) (j) (k) (l)
2019-07-28 Smoke in Siberia

(m) (n) (o) (p)
2018-11-10 US Camp Fire smoke

(q) (r) (s) (t)
2020-09-09 Smoke in Western US

(u) (v) (w) (x)
2020-06-18 Dust in Tropical Atlantic Ocean

(y) (z) (α) (β)
2019-03-02 Dust in Tropical Atlantic Ocean

(caption on next page)

**Fig. 7.** The retrieved AOCH-$O_2$AB for seven selected cases (seven rows) and comparison with ALH-$O_2$A and CALIOP L1B backscatter profiles. The first column shows true color images from corresponding VIIRS/Suomi-NPP granules, in which the red lines are the CALIOP tracks. The retrieved AOCH from our $O_2$AB algorithm for each case is shown in the second column, while the third column illustrates the retrieved ALH from the $O_2$A algorithm (TROPOMI operational Level 2 products) but relative to the surface. The CALIOP level 1B total attenuated backscatter curtain plots at 532 nm are shown in the last column, where the cyan and magenta lines represent the collocated mean TROPOMI retrieved AOCH-$O_2$AB and ALH-$O_2$A within $3 \times 3$ retrieval pixels of each CALIOP footprint. The error bar for TROPOMI ALH represents the standard deviation for these $3 \times 3$ retrieval pixels. (For interpretation of the references to color in this figure legend, the reader is referred to the web version of this article.)

and w). In contrast, the dust plume on 2 March 2019 is not far from its source, resulting in a plume height located in the boundary layer ($< 2$ km). Both AOCH-$O_2$AB and ALH-$O_2$A retrievals are close to CALIOP along its track (Fig. 7β), while the largest AOCH-$O_2$AB is still ~0.5 km higher than ALH-$O_2$A (Fig. 7z and α).

Generally, AOCH-$O_2$AB from our retrieval algorithm is 1–3 km higher than that of the TROPOMI ALH-$O_2$A product for all study cases. We presume it is not only related to the additional $O_2$ B band observations used in our retrieval, but also reflects different aerosol model

assumptions and other details of the two algorithms. Quantitative understanding of these differences can be investigated in the future studies. The comparison with the CALIOP total attenuated backscatter profile at 532 nm indicates that AOCH-$O_2$AB is closer to the central height with the strongest backscatter of CALIOP, while ALH-$O_2$A is lower.

### 3.2. Validation and intercomparison

For all the cases studied in Section 3.1, the retrieved AOD and AOCH
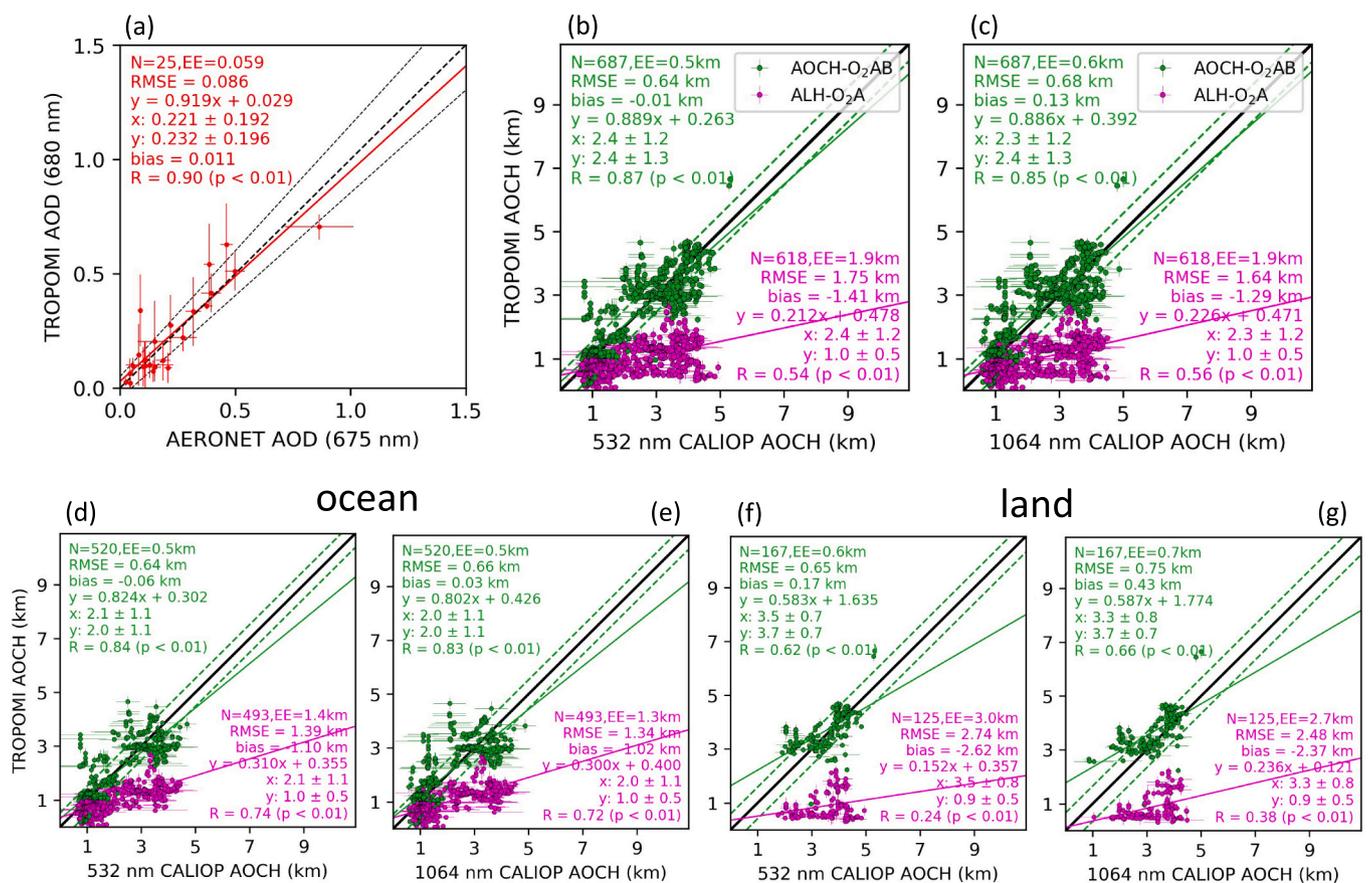


**Fig. 8.** Comparison of TROPOMI AOD and AOCH retrieved from our $O_2$AB retrieval algorithm, as well as ALH from the $O_2$A operational algorithm, with the corresponding AERONET and CALIOP measurements pixel by pixel for all cases in Fig. 7. (a) Scatterplot of TROPOMI 680 nm AOD versus AERONET 675 nm AOD, collocated at the AERONET sites. Due to the lack of valid collocated data, there are no datapoints for two of the seven cases shown in this panel. The dotted lines in this panel represent error envelops, i.e., $\pm(0.05 + 10\%)$ AOD error. The error bar of AERONET AOD is the standard deviation of AERONET products within $\pm 1$ h of the TROPOMI overpass time, while the TROPOMI AOD error bar represents the standard deviation within a 0.5° circle corresponding to AERONET sites. (b) Scatterplot of collocated TROPOMI ALH within $3 \times 3$ retrieval pixels of each CALIOP footprint versus CALIOP AOCH defined by Eq. (6) using aerosol extinction at 532 nm. Green markers represent AOCH-$O_2$AB, and magenta markers represent ALH-$O_2$A. (c) Same as panel (b) but for CALIOP AOCH calculated by aerosol extinction at 1064 nm. (d) and (e) Same as panels (b) and (c) but for cases over ocean. (f) and (g) Land pixels results. Also annotated are the one-to-one line (solid black line), linear regression fit (red line in panel (a) and green and magenta lines in panels (b-g)), number of scatter points (N), the error envelop within which 67% ($1\sigma$) of datapoints are (EE) (dashed green lines in panel (b-g)), root mean square error (RMSE), mean bias, linear regression equation, mean value and standard deviation of x-axis and y-axis data, correlation coefficient (R), and significance level (P). The error bar for TROPOMI AOCH represents the standard deviation for an array of $3 \times 3$ retrieval pixels, while that for CALIOP AOCH represents the standard deviation of over five adjacent CALIOP 5 km footprints. As mentioned in the text, the heights in this figure are all above mean sea level. (For interpretation of the references to color in this figure legend, the reader is referred to the web version of this article.)

from our O$_2$AB retrieval algorithm were validated with the AERONET AOD products and CALIOP level 2 5 km aerosol extinction profiles quantitatively in this section. Besides, the two retrievals, AOCH-O$_2$AB and ALH-O$_2$A for all cases are also compared statistically here.

As shown in Fig. 8a, the mean values of TROPOMI AOD at those pixels within 0.5° of AERONET sites for each case in Fig. 7 are compared with AERONET AOD, which are also averaged between 1 h before and after the TROPOMI overpassed time. The error bars represent the corresponding standard deviation. To maintain the temporal consistency in AERONET data and spatial consistency in TROPOMI, only the points with standard deviation smaller than 0.2 for both AERONET AOD and TROPOMI AOD are shown in the scatterplot. It is clear that our TROPOMI AOD retrieval has good agreement with AERONET AOD, with 0.9 correlation coefficient, 0.011 bias and 0.086 root-mean-square-error (RMSE). Around 67% TROPOMI AOD retrieval has the error smaller than 0.059 compared with AERONET AOD. The collocated AOD pairs, with limited data samplings, show over 72% falling in an uncertainty envelope of ±(0.05 + 10%AOD), similar to and at times improved over the uncertainty of the MODIS C5 AOD product over land (±0.05 + 15% AOD) (Levy et al., 2010).

For ALH quantitative validation, based on previous studies (Koffi et al., 2012; Nanda et al., 2020; Xu et al., 2017; Xu et al., 2019), CALIOP level 2 aerosol extinction profiles at both 532 nm and 1064 nm are used to calculate an aerosol weighted extinction height defined in Eq. (6) as AOCH$_{CALIOP}$:

$$AOCH_{CALIOP} = \frac{\sum_{i=1}^{n} \beta_{ext,i} Z_i}{\sum_{i=1}^{n} \beta_{ext,i}}. \tag{6}$$

Here, $\beta_{ext,i}$ represents the aerosol extinction coefficient (km$^{-1}$) at vertical level $i$, whose altitude is $Z_i$. As a result, AOCH$_{CALIOP}$ describes the altitude at which the aerosol extinction coefficient is the largest, consistent with the definition of AOCH in our aerosol model assumption. As described in our previous study (Xu et al., 2019), to compensate for the bias resulting from "clear air", whose extinction coefficient is zero in CALIOP products and may be inaccurate, an exponentially decayed background aerosol extinction profile with 0.07 columnar AOD at 532 nm is added when deriving AOCH$_{CALIOP}$. Considering the weaker backscatter signal at longer wavelength, the lidar can even detect signals even below the strong aerosol scattering layers at 1064 nm, which are difficult to penetrate at 532 nm. Therefore, we validate TROPOMI ALH with AOCH$_{CALIOP}$ calculated from aerosol extinction at both 532 nm and 1064 nm.

In Fig. 8b and c, the green markers and lines represent AOCH-O$_2$AB, while magenta represents ALH-O$_2$A. It is clear that AOCH-O$_2$AB has a

better agreement with ALH$_{CALIOP}$ at 532 nm with an RMSE of 0.64 km and a correlation coefficient R of 0.87 (0.68 km RMSE and 0.85 R for 1064 nm AOCH$_{CALIOP}$) than ALH-O$_2$A, whose RMSE is 1.75 km and R is 0.54. Even though when compared with AOCH$_{CALIOP}$ at 1064 nm, the ALH-O$_2$A RMSE is lower and R becomes higher, this product still has less agreement than AOCH-O$_2$AB. In general, our retrieved AOCH-O$_2$AB shows ~0.5 km difference when compared with AOCH$_{CALIOP}$, indicating an improved performance over ALH-O$_2$A that is always underestimated (as shown in previous studies). To further analyze the retrieval performance on different surface types, we validate the ocean and land pixels separately in Fig. 8d, e and f, g. Over ocean, both the AOCH-O$_2$AB ($R >$ 0.8) and ALH-O$_2$A ($R >$ 0.7) have high correlation with AOCH$_{CALIOP}$, whereas the ALH-O$_2$A errors (RMSE >1 km, bias $< -1$ km) are larger than in our AOCH-O$_2$AB retrieval. For land surfaces, although both the AOCH-O$_2$AB and ALH-O$_2$A have degraded performance than over the ocean surfaces, the AOCH-O$_2$AB still shows low errors (~0.7 km RMSE, $<$ 0.5 km bias) and high correlation coefficient ($R >$ 0.6) while the ALH-O$_2$A presents errors twice to ocean cases and little correlation with AOCH$_{CALIOP}$ ($R <$ 0.4).

The probability density histograms of the differences between AOCH-O$_2$AB, ALH-O$_2$A and AOCH$_{CALIOP}$ retrievals for co-located pixels of all cases in Fig. 7 and their statistics are presented in Fig. 9. Green, magenta and blue represent the ΔAOCH equal to AOCH-O$_2$AB −AOCH$_{CALIOP}$, ALH-O$_2$A −AOCH$_{CALIOP}$ and AOCH-O$_2$AB−ALH-O$_2$A, respectively. It is clear from Fig. 9a that the AOCH-O$_2$AB retrieval is close to AOCH$_{CALIOP}$ with 0.13 km ΔAOCH on average, smaller than the mean bias of ALH-O$_2$A (−1.29 km). More than 75% of AOCH-O$_2$AB retrievals have <0.7 km bias when compared to AOCH$_{CALIOP}$, while the 75th percentile of ΔAOCH between ALH-O$_2$A and AOCH$_{CALIOP}$ is ~2 km. Moreover, ALH-O$_2$A is lower than AOCH$_{CALIOP}$ (negative ΔAOCH) for nearly every case, but ΔAOCH between AOCH-O$_2$AB and AOCH$_{CALIOP}$ displays normal distribution, indicating a quasi-random retrieval error of AOCH-O$_2$AB. AOCH-O$_2$AB is found to be ~1.6 km higher than ALH-O$_2$A on average. Fig. 9b and c show the statistical histograms for ocean and land pixels, respectively. Even though the mean bias of AOCH-O$_2$AB for land surfaces is higher than for ocean (0.43 km), it is still far less than the bias in the counterpart (−2.37 km) of ALH-O$_2$A retrievals, indicating the improvement of our algorithm especially over land. In summary, AOCH-O$_2$AB is much closer to AOCH$_{CALIOP}$ than ALH-O$_2$A. Our algorithm, which adds the O$_2$ B band, improves ALH retrieval both over the ocean and land, although the improvement over land surfaces is more significant.
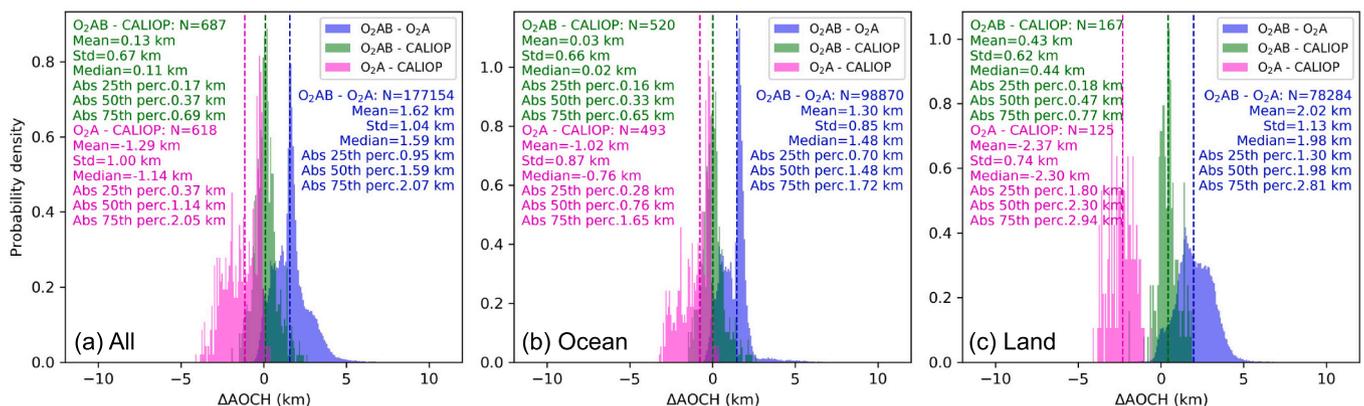


**Fig. 9.** The histograms of the difference between any two of the co-located AOCH-O$_2$AB, ALH-O$_2$A and AOCH$_{CALIOP}$ (ΔAOCH), as well as their statistics, including the total number of datapoints (N), the mean value (Mean) and standard deviation (Std), the median value (Median), the 25th, 50th, and 75th percentiles of the absolute values (25th perc., 50th perc., and 75th perc.). Panel (a) includes all cases in Fig. 7 while (b) and (c) are summaries of ocean and land pixels, respectively. The dashed lines represent median values. The co-located ALH-O$_2$A are resampled to match the spatial resolution of AOCH-O$_2$AB. The datapoints of the difference between AOCH-O$_2$AB (or ALH-O$_2$A) and AOCH$_{CALIOP}$ are the same as Fig. 8c. The AOCH$_{CALIOP}$ in this figure is also for 1064 nm.

## 4. The application of AOCH in PM$_{2.5}$ modeling

Although the satellite-retrieved AOCH does not contain the detailed aerosol profile information at multiple altitude levels, here we illustrate its potential application for improving surface PM$_{2.5}$ estimation. Full application of AOCH together with AOD for surface PM$_{2.5}$ air quality monitoring warrants future investigation in conjunction with more sophisticated modeling and analysis. A pilot study is presented below to apply the TROPOMI AOCH-O$_2$AB observations to improve surface PM$_{2.5}$ reported in the MERRA-2 re-analysis data that are generated by the assimilation of AOD but without any observational constraint of the aerosol vertical profile.

A smoke plume transport event from the west of North America to the southeast was selected for investigation. As evident in the VIIRS true color image on 16–18 August 2018 (Fig. 10a), this smoke plume was optically thick with significant day-to-day spatial variability. We retrieved the AOCH from TROPOMI measurements for this case and showed its spatial distribution overlaid by the surface PM$_{2.5}$ concentrations from EPA sites (colored dots in Fig. 10b). The simultaneous AOD retrieval (Fig. 10d) is lower than the VIIRS deep blue AOD (Fig. 10e), but consistent with AERONET AOD products (colored dots in Fig. 10d). In Fig. 10b, the TROPOMI AOCH-O$_2$AB ranges from 2 km up to 6 km and higher, illustrating different vertical distributions across the plume. For instance, those pixels shown by the pink arrows in Fig. 10b and d have AOD > 1.0, but AOCH are around 2–3 km. This means that most smoke particles concentrate in the lower atmosphere, close to the boundary layer. Given that smoke aerosol is fine mode dominated, the surface PM$_{2.5}$ concentration in these regions, therefore, are expected to be high. Indeed, EPA PM$_{2.5}$ is always larger than 80 µg/m$^3$ here. On the contrary, for those pixels denoted by green arrows, despite the high AOD similar to pink arrow regions, their AOCH are much higher (> 5 km). As a result, the EPA surface PM$_{2.5}$ show low values (< 20 µg/m$^3$). Unfortunately, the

ALH-O$_2$A product (Fig. 10c) misses the retrieval of the heavy plume transported to high altitude (green arrows in Fig. 10b and d). Moreover, the ALH-O$_2$A is 2–4 km lower than AOCH$_{CALIOP}$ for this case, so it is not used in the following PM$_{2.5}$ study. This case qualitatively supports that our satellite AOCH retrievals have merit for estimating regional or global surface PM$_{2.5}$ concentration, hence compensating for the limited spatial coverage of PM$_{2.5}$ observation from in situ sites.

Quantitatively, we applied the AOCH-O$_2$AB to improve the surface PM$_{2.5}$ re-analysis from MERRA-2. As introduced by Buchard et al. (2017), the MERRA-2 modeling system uses the GEOS-5 Earth system model (Molod et al., 2015; Rienecker et al., 2008), which is radiatively coupled to the Goddard Chemistry Aerosol Radiation and Transport model (GOCART) (Chin et al., 2002; Colarco et al., 2010). It simulates three-dimensional mass concentration of five types of aerosols including dust, sea salt, sulfate, and black and organic carbon (BC and OC) with 0.5° × 0.625° spatial resolution and 72 hybrid-eta layers from the surface to 0.01 hPa. The AOD is derived from the sum of the aerosol extinction coefficients of all species at each vertical level, which are converted from mass concentration based on the assumed optical properties (Colarco et al., 2010). According to the particle size of each aerosol species in the model, fine aerosols near the surface with aerodynamic diameters less than 2.5 µm, known as PM$_{2.5}$, can also be derived as model output. Both space-based AOD (e.g., MODIS, AVHRR, and MISR) and ground-based AOD (AERONET) are assimilated in MERRA-2, but the lack of constraints on aerosol vertical distribution in the assimilation may result in the biases in the surface PM$_{2.5}$. Although the evaluation of the MERRA-2 total (aerosol plus molecular) attenuated backscatter coefficient against independent CALIOP backscatter profiles exhibits a similar seasonal averaged vertical structure over important aerosol source regions, it is possible for MERRA-2 to miss some lidar-detected aerosol layers above the boundary layer that are likely due to long-range smoke transport in specific cases (Buchard et al., 2017). The
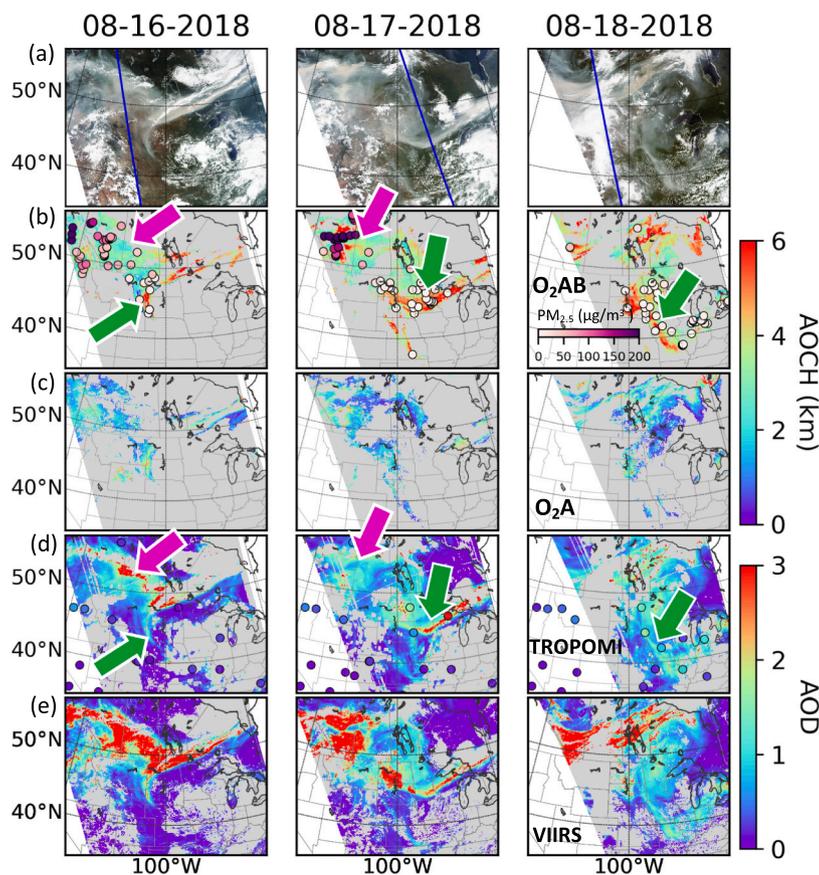


**Fig. 10.** Multiple satellite data products and surface observations of a smoke transport event on 08/16 (left column), 08/17 (middle), and 08/18 (right) 2018, including VIIRS true color image (first row), spatial distributions of AOCH-O$_2$AB (second row) overlaid with hourly surface PM$_{2.5}$ data (color-coded dots), ALH-O$_2$A from TROPOMI operational Level 2 products (third row), AOD at 680 nm retrieved by this study (fourth row) overlaid with AEROENT AOD at 675 nm, and VIIRS AOD product at 670 nm (fifth row). The blue lines in (a) are the ground tracks of CALIOP. The surface PM$_{2.5}$ data is obtained at sites from Environment and Climate Change Canada (ECCC) and the United States Environmental Protection Agency (EPA). Both surface PM$_{2.5}$ and AOD data are shown for the time when TROPOMI overpasses the sites. (For interpretation of the references to color in this figure legend, the reader is referred to the web version of this article.)

comparison of monthly mean MERRA-2 $PM_{2.5}$ with observations from the EPA and the Interagency Monitoring of Protected Visual Environments (IMPROVE) networks also indicates that $PM_{2.5}$ biases from MERRA-2 may appear in the eastern US in summer (Buchard et al., 2016; Buchard et al., 2017).

Here we use a scaling method to quantitively show the potential of AOCH for improving $PM_{2.5}$ re-analysis. First, similar to $AOCH_{CALIOP}$ shown above, an aerosol extinction weighted height for MERRA-2 data, $AOCH_M$, is computed following Eq. (6). For each grid, the $\beta_{ext,\,i}$ is the sum of the extinction coefficients for all aerosol species at level $i$, which can be calculated from the MERRA-2 three-dimensional aerosol mixing ratio data and the mass extinction efficiency of each aerosol type (Colarco et al., 2010) as follows:

$$\beta_{ext,i} = \sum_{j=1}^{m} \beta_{ext,i,j} = \sum_{j=1}^{m} \alpha_{i,j}\rho_i q_{ext,j}. \tag{7}$$

Here, $\alpha_{i,\,j}$ is the mixing ratio at level $i$ for aerosol type $j$, and $q_{ext,\,j}$ represents the mass extinction efficiency of this aerosol type. $\rho_i$ is the air density at level $i$, and $m$ shows the total number of aerosol species. To distinguish it from AOCH from MERRA-2 ($AOCH_M$), $AOCH_T$ is used for short to represent TROPOMI AOCH-$O_2AB$ retrieval in the following parts, where ALH-$O_2A$ is not analyzed. Due to the lack of aerosol vertical distribution observations in the data assimilation, $AOCH_M$ is often close to the boundary layer height and is inconsistent with elevated aerosols for the long-range smoke transport case as in Fig. 10. Thus, the differences ($\Delta AOCH$) between $AOCH_M$ and satellite-observed $AOCH_T$ are remarkable, in the range of 1–4 km (color bar in Fig. 11a or c). As a result, the surface $PM_{2.5}$ concentration is overestimated in MERRA-2 for this smoke case (Fig. 11a). From the spatial distribution of MERRA-2 $PM_{2.5}$ (Fig. 11b), it is clear that large errors when compared with EPA

indicates that the high bias of MERRA-2 $PM_{2.5}$ is significantly reduced in those regions with green arrows in Fig. 10. All of the three-hourly MERRA-2 data and hourly EPA data used in this section are interpolated at the time TROPOMI overpasses before comparison.

In general, although the AOCH retrieved from satellite has uncertainty, it provides effective and valuable information about aerosol vertical distribution that is currently lacking in space-borne measurements. From the case study, it is deduced that global distribution of AOCH also has the potential to help improve surface $PM_{2.5}$ concentration, especially for elevated aerosols with long-distance transportation. The correction method and the threshold definitions shown here are meant to be illustrative and conceptual, and a full investigation of AOCH applications to surface $PM_{2.5}$ air quality monitoring deserves a separate study.

## 5. Conclusions and discussions

In this study, we described the development of an algorithm to retrieve aerosol optical central height (AOCH) over dark targets from TROPOMI measurements using not only the $O_2$ A band (763 nm) but also the $O_2$ B band at shorter wavelength (688 nm). Due to the lower surface reflectance in the $O_2$ B band, especially over vegetation, it has the capability to compensate for the large impact of the uncertainty of surface reflectance on aerosol retrieval from the $O_2$ A band. Based on our previous algorithm developed for EPIC/DSCOVR AOCH retrieval using these two $O_2$ absorption bands, we adjusted and improved the algorithm for TROPOMI hyperspectral measurements processing in the following ways: (1) convolved the TROPOMI hyperspectral measurements into narrow-band TOA radiances ranging from UV to SWIR using a spectral response function with coarser FWHM, then used these narrow-band

$$PM_{2.5,Mc} = \begin{cases} PM_{2.5,M0}, & AOD_M < 0.7 \text{ and} \Delta AOCH < 2 \text{ km} \\ PM_{2.5,M0} \times \dfrac{AOD_T}{AOD_M} \times \dfrac{AOCH_M}{AOCH_T}, & AOD_M < 0.7 \text{ and } 2 \text{ km} \le \Delta AOCH < 2.5 \text{ km} \\ PM_{2.5,M0} \times \dfrac{AOCH_M}{AOCH_T}, & AOD_M \ge 0.7 \text{ or} \Delta AOCH \ge 2.5 \text{ km} \end{cases} \tag{8}$$

$PM_{2.5}$ are found in those regions with large AOD and high $AOCH_T$ (green arrow regions in Fig. 10), where the difference between $AOCH_M$ and $AOCH_T$ is large.

Therefore, next, a step-wise scaling factor scheme is conceived based on the values of $\Delta AOCH = AOCH_T - AOCH_M$ and AOD for each pixel, and is used to correct MERRA-2 $PM_{2.5}$:

where $PM_{2.5,\,Mc}$ indicates MERRA-2 $PM_{2.5}$ data after correction from the original data $PM_{2.5,\,M0}$. One threshold is defined for MERRA-2 AOD ($AOD_M$, 0.7), along with the two thresholds of $\Delta AOCH$ (2 km, 2.5 km) to distinguish different circumstances where different scaling factors are used. For those pixels where both $AOD_M < 0.7$ and $\Delta AOCH < 2$ km, the MERRA-2 $PM_{2.5}$ are close to the EPA measurements, so no correction is applied. If the $AOD_M$ is still small but $\Delta AOCH$ is larger than 2 km and smaller than 2.5 km, both AOD ratio and AOCH ratio between TROPOMI and MERRA-2 are used to correct MERRA-2 $PM_{2.5}$. For other pixels, where $AOD_M$ is large or $\Delta AOCH$ is larger than 2.5 km, the difference in AOD between MERRA-2 and TROPOMI has less impact on $PM_{2.5}$ concentration, so only the AOCH ratio is used in the correction. After applying this correction method, MERRA-2 $PM_{2.5}$ in this smoke plume has a higher correlation coefficient ($R = 0.88$) and lower RMSE (RMSE = 17.866 μg/m$^3$, Fig. 11c) than the original data ($R = 0.69$, RMSE = 48.567 μg/m$^3$, Fig. 11a). The spatial distribution in Fig. 11d also

observations in all retrieval steps; (2) updated the surface reflectance using climatology of 10-year MODIS surface products to reduce the uncertainty from their atmospheric correction over land and selected dark targets based on NDVI; (3) developed a new cloud mask strategy suitable for TROPOMI channels based on the spectral slope of TOA radiances; (4) created a method to classify dust and smoke particles from absorbing aerosols using the ratio of aerosol path radiance in the blue and SWIR bands; (5) updated the LUT for smoke particles according to the statistics of AERONET inversion products for recent smoke events (2018–2019) in the US and applied different LUTs in dust or smoke plume retrieval.

After applying our two-band retrieval algorithm to several smoke and dust plume cases from 2018 to 2020 around the world, the retrieved AOCH-$O_2AB$ is compared with TROPOMI operational level 2 ALH product (ALH-$O_2A$) and CALIOP backscatter profile. For all cases, AOCH-$O_2AB$ is found to be ~1.6 km higher than ALH-$O_2A$ on average and systematically closer to the central height with the strongest backscatter of CALIOP, effectively removing the 2 km low bias found in the ALH-$O_2A$ product over land. By defining an extinction weighted aerosol height from CALIOP aerosol extinction profile products ($AOCH_{CALIOP}$), the quantitative validation at pixels along the CALIOP track illustrates that AOCH-$O_2AB$ is more consistent with $AOCH_{CALIOP}$ than ALH-$O_2A$, with a higher correlation coefficient (R is 0.85–0.87) and lower errors
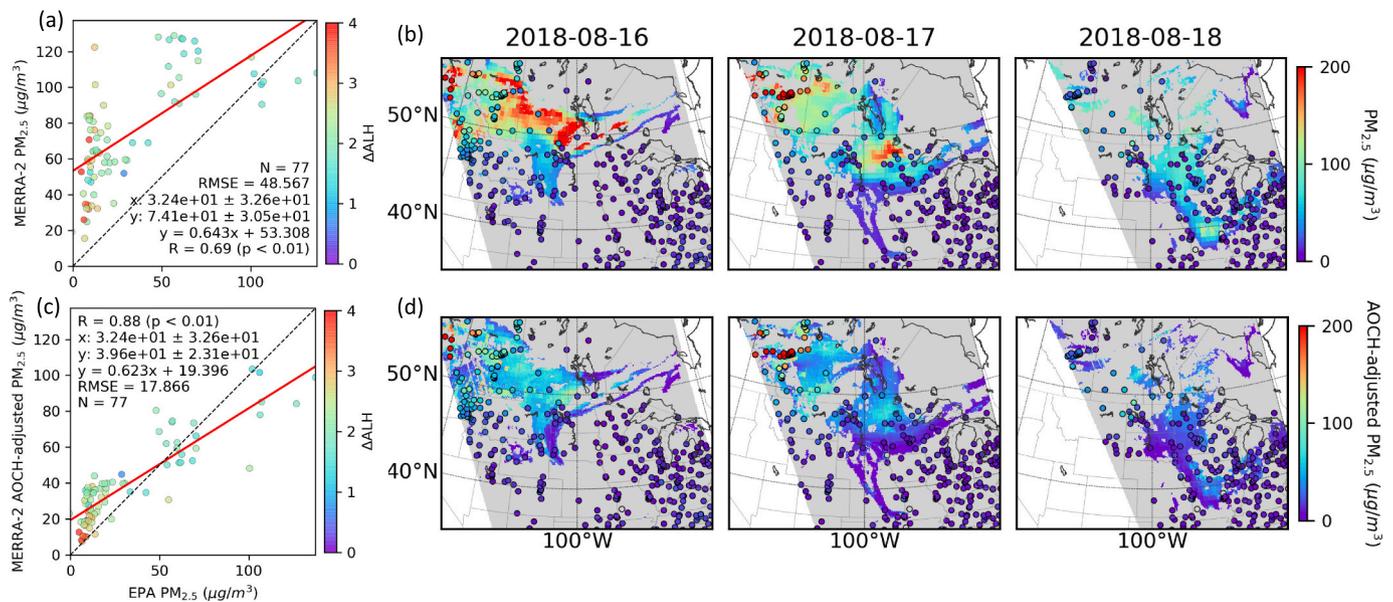
**Fig. 11.** The comparison of MERRA-2 PM$_{2.5}$ data for the case in Fig. 10 with hourly surface PM$_{2.5}$ measurements from EPA sites before and after correction using TROPOMI AOCH-O$_2$AB retrievals. (a) Scatterplot of PM$_{2.5}$ from MERRA-2 and EPA measurements without any correction. The color of each datapoint represents the ALH difference (TROPOMI AOCH-O$_2$AB – MERRA-2 ALH). The red line shows linear regression fitting. The EPA measurements are picked up at TROPOMI overpass time, and the MERRA-2 data is the mean value of pixels within 0.5° circle around each EPA site. (b) The map of MERRA-2 (background color sampled over the smoke areas where AOD and AOCH-O$_2$AB are retrieved in Fig. 10) and EPA PM$_{2.5}$ (dots) at TROPOMI overpass time. Row (c) is the same as panel (a) but after correcting MERRA-2 PM$_{2.5}$ using TROPOMI AOCH-O$_2$AB. Row (d) is also the same as panel (b) but with AOCH correction. (For interpretation of the references to color in this figure legend, the reader is referred to the web version of this article.)

(RMSE is ~0.6 km, mean bias is 0.13 km). Even though the correlations of our AOCH-O$_2$AB over land are weaker than those over ocean, the errors are still low (RMSE is ~0.7 km, mean bias <0.5 km) and better than ALH-O$_2$A whose quality is much low over land. The better performance of our algorithm when compared to the TROPOMI operational products over both ocean and land indicates the improvement of adding the O$_2$ B band in ALH retrieval, especially over land.

Finally, a possible application of TROPOMI-retrieved AOCH-O$_2$AB is shown to adjust the surface PM$_{2.5}$ concentration from MERRA-2 reanalysis data for an elevated smoke plume case in North America. When compared with the in situ data measured at EPA sites, the surface PM$_{2.5}$ is overestimated by MERRA-2 for this case with long-range transport. By using a scaling method, the MERRA-2 PM$_{2.5}$ is corrected quantitatively by the ratio of MERRA-2 aerosol extinction weighted height and TROPOMI AOCH-O$_2$AB. As a result, the AOCH-adjusted MERRA-2 PM$_{2.5}$ has better agreement with EPA data and the correlation coefficient is improved from 0.69 to 0.88, while the RMSE is reduced from ~50 μg/m$^3$ to ~20 μg/m$^3$.

The algorithm developed in this study is appropriate for dark targets classified by the NDVI. Over bright surfaces, the thresholds defined in the cloud mask and aerosol type classification strategy must be reconsidered due to the higher surface reflectance and its different spectral dependence. Additionally, the regression coefficients of surface reflectance between the MODIS and TROPOMI channels also differ from this study. Although higher surface reflectance makes it difficult to derive aerosol information from satellite measurements, the surface reflectance in the O$_2$ B band is still lower than in the O$_2$ A band; thus, we believe the combination of the O$_2$ B and A bands benefits the aerosol height retrieval over bright surfaces as well, and this will be studied in the future. Furthermore, although a smoke case in the Eurasia was examined in this study, the smoke LUT summarized from North America smoke events in our algorithm may not be representative for worldwide wildfires or other fires. Thus, more LUTs representing different smoke characteristics will be required to make our algorithm operational in the future. Adding other LUTs simulated for a scattering aerosol model could also expand our algorithm to include non-absorbing aerosols. Moreover, the

comparison with CALIOP aerosol profiles in this study is still limited to several case studies. We will apply our algorithm to more cases and compare the results with other possible aerosol profile measurements to summarize the statistical performance of our algorithm. The thresholds defined in cloud mask and the classification of dust and smoke aerosols deserves more tests and may be adjusted when expanded globally. The diverse aerosol vertical distribution shape assumptions may also cause some discrepancy in the ALH retrievals; this also deserves more studies in the future. Last but not least, the usage of satellite aerosol height retrieval in the correction of surface PM$_{2.5}$ in this study merely shows a potential application of aerosol height; it may be extended in many other ways or fields, such as being involved in a data assimilation system or trained by a machine learning method to predict surface PM$_{2.5}$. In conclusion, our retrieval algorithm provides a reliable aerosol height retrieval by adding the O$_2$ B band to O$_2$ A band measurements from TROPOMI for the first time and has the capability to be applied in other instruments with O$_2$ A and/or B absorption bands.

## Declaration of Competing Interest

The authors declare that they have no known competing financial interests or personal relationships that could have appeared to influence the work reported in this paper.

## Appendix A. Supplementary data

Supplementary data to this article can be found online at https://doi.org/10.1016/j.rse.2021.112674.

## References

Buchard, V., et al., 2016. Evaluation of the surface PM2.5 in version 1 of the NASA MERRA aerosol reanalysis over the United States. Atmos. Environ. 125, 100–111.
Buchard, V., et al., 2017. The MERRA-2 aerosol reanalysis, 1980 onward. Part II: evaluation and case studies. J. Clim. 30, 6851–6872.
Carboni, E., et al., 2007. Retrieval of aerosol properties from SEVIRI using visible and infrared channels. In: Proceedings of EUMETSAT/AMS conference.
Chimot, J., et al., 2017. An exploratory study on the aerosol height retrieval from OMI measurements of the 477 nm O2 − O2 spectral band using a neural network approach. Atmos. Measure. Tech. 10, 783–809.
Chin, M., et al., 2002. Tropospheric aerosol optical thickness from the GOCART model and comparisons with satellite and sun photometer measurements. J. Atmos. Sci. 59, 461–483.
Christian, K., Wang, J., Ge, C., Peterson, D., Hyer, E., Yorks, J., McGill, M., 2019. Radiative forcing and stratospheric warming of pyrocumulonimbus smoke aerosols: first modeling results with multisensor (EPIC, CALIPSO, and CATS) views from space. Geophys. Res. Lett. 46, 10061–10071.
Ciren, P., Kondragunta, S., 2014. Dust aerosol index (DAI) algorithm for MODIS. J. Geophys. Res.-Atmos. 119, 4770–4792.
Colarco, P., da Silva, A., Chin, M., Diehl, T., 2010. Online simulations of global aerosol distributions in the NASA GEOS-4 model and comparisons to satellite and ground-based aerosol optical depth. J. Geophys. Res.-Atmos. 115.
Colosimo, S.F., Natraj, V., Sander, S.P., Stutz, J., 2016. A sensitivity study on the retrieval of aerosol vertical profiles using the oxygen A-band. Atmos. Meas. Tech. 9, 1889–1905.
Corradini, S., Cervino, M., 2006. Aerosol extinction coefficient profile retrieval in the oxygen A-band considering multiple scattering atmosphere. Test case: SCIAMACHY nadir simulated measurements. J. Quant. Spectrosc. Radiat. Transf. 97, 354–380.
Ding, S., Wang, J., Xu, X., 2016. Polarimetric remote sensing in oxygen a and B bands: sensitivity study and information content analysis for vertical profile of aerosols. Atmos. Measure. Tech. 9, 2077–2092.
Dubuisson, P., Frouin, R., Dessailly, D., Duforêt, L., Léon, J.-F., Voss, K., Antoine, D., 2009. Estimating the altitude of aerosol plumes over the ocean from reflectance ratio measurements in the O2 A-band. Remote Sens. Environ. 113, 1899–1911.
Ford, B., Heald, C.L., 2012. An A-train and model perspective on the vertical distribution of aerosols and CO in the Northern Hemisphere. J. Geophys. Res.-Atmos. 117 n/a-n/a.
Frankenberg, C., Hasekamp, O., O'Dell, C., Sanghavi, S., Butz, A., Worden, J., 2012. Aerosol information content analysis of multi-angle high spectral resolution measurements and its benefit for high accuracy greenhouse gas retrievals. Atmos. Measure. Tech. 5, 1809–1821.
Gabella, M., Kisselev, V., Perona, G., 1999. Retrieval of aerosol profile variations from reflected radiation in the oxygen absorption A band. Appl. Opt. 38, 3190–3195.
Geddes, A., Bösch, H., 2015. Tropospheric aerosol profile information from high-resolution oxygen A-band measurements from space. Atmos. Measure. Tech. 8, 859–874.
Griffin, D., et al., 2020. The 2018 fire season in North America as seen by TROPOMI: aerosol layer height intercomparisons and evaluation of model-derived plume heights. Atmos. Measure. Tech. 13, 1427–1445.
Hollstein, A., Fischer, J., 2014. Retrieving aerosol height from the oxygen a band: a fast forward operator and sensitivity study concerning spectral resolution, instrumental noise, and surface inhomogeneity. Atmos. Measure. Tech. 7, 1429–1441.
Hou, W., Wang, J., Xu, X., Reid, J.S., 2017. An algorithm for hyperspectral remote sensing of aerosols: 2. Information content analysis for aerosol parameters and principal components of surface spectra. J. Quant. Spectrosc. Radiat. Transf. 192, 14–29.
Hsu, N.C., Tsay, S.C., King, M.D., Herman, J.R., 2006. Deep blue retrievals of Asian aerosol properties during ACE-Asia. IEEE Trans. Geosci. Remote Sens. 44, 3180–3195.
Hsu, N.C., et al., 2013. Enhanced deep blue aerosol retrieval algorithm: the second generation. J. Geophys. Res.-Atmos. 118, 9296–9315.

Kaufman, Y.J., Tanré, D., Remer, L.A., Vermote, E.F., Chu, A., Holben, B.N., 1997. Operational remote sensing of tropospheric aerosol over land from EOS moderate resolution imaging spectroradiometer. J. Geophys. Res.-Atmos. 102, 17051–17067.
Koch, D., Del Genio, A.D., 2010. Black carbon semi-direct effects on cloud cover: review and synthesis. Atmos. Chem. Phys. 10, 7685–7696.
Koffi, B., et al., 2012. Application of the CALIOP layer product to evaluate the vertical distribution of aerosols estimated by global models: AeroCom phase I results. J. Geophys. Res.-Atmos. 117.
Koffi, B., et al., 2016. Evaluation of the aerosol vertical distribution in global aerosol models through comparison against CALIOP measurements: AeroCom phase II results. J. Geophys. Res.-Atmos. 121, 7254–7283.
Kokaly, R.F., et al., 2017. USGS Spectral Library Version 72327-638X.
Kokhanovsky, A.A., Rozanov, V.V., 2010. The determination of dust cloud altitudes from a satellite using hyperspectral measurements in the gaseous absorption band. Int. J. Remote Sens. 31, 2729–2744.
Levy, R.C., Remer, L.A., Kleidman, R.G., Mattoo, S., Ichoku, C., Kahn, R., Eck, T.F., 2010. Global evaluation of the collection 5 MODIS dark-target aerosol products over land. Atmos. Chem. Phys. 10, 10399–10420.
Lyapustin, A., Wang, Y., Korkin, S., Kahn, R., Winker, D., 2020. MAIAC thermal technique for smoke injection height from MODIS. IEEE Geosci. Remote Sens. Lett. 17, 730–734.
Martins, J.V., Tanré, D., Remer, L., Kaufman, Y., Mattoo, S., Levy, R., 2002. MODIS cloud screening for remote sensing of aerosols over oceans using spatial variability. Geophys. Res. Lett. 29. MOD4-1-MOD4-4.
Molod, A., Takacs, L., Suarez, M., Bacmeister, J., 2015. Development of the GEOS-5 atmospheric general circulation model: evolution from MERRA to MERRA2. Geosci. Model Dev. 8, 1339–1356.
Nanda, S., et al., 2018. A weighted least squares approach to retrieve aerosol layer height over bright surfaces applied to GOME-2 measurements of the oxygen A band for forest fire cases over Europe. Atmos. Measure. Tech. 11, 3263–3280.
Nanda, S., De Graaf, M., Veefkind, J.P., Ter Linden, M., Sneep, M., De Haan, J., Levelt, P. F., 2019. A neural network radiative transfer model approach applied to the tropospheric monitoring instrument aerosol height algorithm. Atmos. Measure. Tech. 12, 6619–6634.
Nanda, S., de Graaf, M., Veefkind, J.P., Sneep, M., ter Linden, M., Sun, J., Levelt, P.F., 2020. A first comparison of TROPOMI aerosol layer height (ALH) to CALIOP data. Atmos. Meas. Tech. 13, 3043–3059.
O'Dell, C.W., et al., 2018. Improved retrievals of carbon dioxide from orbiting carbon observatory-2 with the version 8 ACOS algorithm. Atmos. Measure. Tech. 11, 6539–6576.
Park, S.S., Kim, J., Lee, H., Torres, O., Lee, K.-M., Lee, S.D., 2016. Utilization of O4 Slant Column Density to Derive Aerosol Layer Height from a Spaceborne UV-Visible Hyperspectral Sensor: Sensitivity and Case Study.
Peterson, D.A., Hyer, E., Wang, J., 2014. Quantifying the potential for high-altitude smoke injection in the North American boreal forest using the standard MODIS fire products and subpixel-based methods. J. Geophys. Res.-Atmos. 119, 2013JD021067.
Rienecker, M.M., et al., 2008. The GEOS-5 Data Assimilation System: Documentation of Versions 5.0. 1, 5.1. 0, and 5.2. 0.
Sanders, A.F.J., de Haan, J.F., 2013. Retrieval of aerosol parameters from the oxygen A band in the presence of chlorophyll fluorescence. Atmos. Measure. Tech. 6, 2725–2740.
Sanders, A.F.J., et al., 2015. Evaluation of the operational aerosol layer height retrieval algorithm for sentinel-5 precursor: application to O2 A band observations from GOME-2A. Atmos. Meas. Tech. 8, 4947–4977.
Sanghavi, S., Martonchik, J.V., Landgraf, J., Platt, U., 2012. Retrieval of the optical depth and vertical distribution of particulate scatterers in the atmosphere using O2 A- and B-band SCIAMACHY observations over Kanpur: a case study. Atmos. Meas. Tech. 5, 1099–1119.
Schuster, G.L., et al., 2012. Comparison of CALIPSO aerosol optical depth retrievals to AERONET measurements, and a climatology for the lidar ratio of dust. Atmos. Chem. Phys. 12, 7431–7452.
Skiles, S.M., Painter, T., Okin, G.S., 2017. A method to retrieve the spectral complex refractive index and single scattering optical properties of dust deposited in mountain snow. J. Glaciol. 63, 133–147.
Timofeyev, Y.M., Vasilyev, A.V., Rozanov, V.V., 1995. Information content of the spectral measurements of the 0.76 um O2 outgoing radiation with respect to the vertical aerosol optical properties. Adv. Space Res. 16, 1091–1094.
Torres, O., et al., 2007. Aerosols and surface UV products from ozone monitoring instrument observations: an overview. J. Geophys. Res. 112, 1–14.
Wang, J., Christopher, S.A., 2003. Intercomparison between satellite-derived aerosol optical thickness and PM2.5 mass: implications for air quality studies. Geophys. Res. Lett. 30.
Wang, J., Xu, X., Spurr, R., Wang, Y., Drury, E., 2010. Improved algorithm for MODIS satellite retrievals of aerosol optical thickness over land in dusty atmosphere: implications for air quality monitoring in China. Remote Sens. Environ. 114, 2575–2583.
Wang, J., et al., 2013. Mesoscale modeling of smoke transport over the southeast Asian maritime continent: interplay of sea breeze, trade wind, typhoon, and topography. Atmos. Res. 122, 486–503.
Wang, J., et al., 2014. A numerical testbed for remote sensing of aerosols, and its demonstration for evaluating retrieval synergy from a geostationary satellite constellation of GEO-CAPE and GOES-R. J. Quant. Spectrosc. Radiat. Transf. 146, 510–528.
Wessel, P., Smith, W.H., 1996. A global, self-consistent, hierarchical, high-resolution shoreline database. J. Geophys. Res. Solid Earth 101, 8741–8743.

Winker, D.M., et al., 2009. Overview of the CALIPSO Mission and CALIOP data processing algorithms. J. Atmos. Ocean. Technol. 26, 2310–2323.

Winker, D., Tackett, J., Getzewich, B., Liu, Z., Vaughan, M., Rogers, R., 2013. The global 3-D distribution of tropospheric aerosols as characterized by CALIOP. Atmos. Chem. Phys. 13.

Wu, L., Hasekamp, O., van Diedenhoven, B., Cairns, B., Yorks, J.E., Chowdhary, J., 2016. Passive remote sensing of aerosol layer height using near-UV multiangle polarization measurements. Geophys. Res. Lett. 43, 8783–8790.

Xing, C., et al., 2017. Observations of the vertical distributions of summertime atmospheric pollutants and the corresponding ozone production in Shanghai, China. Atmos. Chem. Phys. 17, 14275–14289.

Xu, X., et al., 2017. Passive remote sensing of altitude and optical depth of dust plumes using the oxygen A and B bands: first results from EPIC/DSCOVR at Lagrange-1 point: aerosol height retrieval from O2 A & B. Geophys. Res. Lett. 44.

Xu, X., Wang, J., Wang, Y., Kokhanovsky, A., 2018a. Chapter 1 - passive remote sensing of aerosol height. In: Islam, T., Hu, Y., Kokhanovsky, A., Wang, J. (Eds.), Remote Sensing of Aerosols, Clouds, and Precipitation. Elsevier, pp. 1–22.

Xu, X., Wang, J., Zeng, J., Hou, W., Meyer, K.G., Platnick, S.E., Wilcox, E.M., 2018b. A pilot study of shortwave spectral fingerprints of smoke aerosols above liquid clouds. J. Quant. Spectrosc. Radiat. Transf. 221, 38–50.

Xu, X., et al., 2019. Detecting layer height of smoke aerosols over vegetated land and water surfaces via oxygen absorption bands: hourly results from EPIC/DSCOVR in deep space. Atmos. Meas. Tech. 12, 3269–3288.

Yang, Z., Wang, J., Ichoku, C., Hyer, E., Zeng, J., 2013. Mesoscale modeling and satellite observation of transport and mixing of smoke and dust particles over northern sub-Saharan African region. J. Geophys. Res.-Atmos. 118, 12,139–112,157.

Zeng, J., Han, Q., Wang, J., 2008. High-spectral resolution simulation of polarization of skylight: sensitivity to aerosol vertical profile. Geophys. Res. Lett. 35.

Zeng, Z.C., et al., 2018. Constraining aerosol vertical profile in the boundary layer using hyperspectral measurements of oxygen absorption. Geophys. Res. Lett. 45, 10,772–710,780.

Zeng, Z.-C., et al., 2020. Constraining the vertical distribution of coastal dust aerosol using OCO-2 O2 A-band measurements. Remote Sens. Environ. 236.